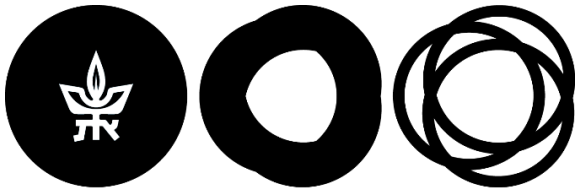

הפקולטה למדעים מדויקים ע"ש ריימונד ובברלי סאקלר

בית הספר לפיסיקה ואסטרונומיה

המחלקה לחומר מעובה

Frequency conversion via composite pulses

In partial fulfillment to the requirements for the degree of

Master of Science at Tel Aviv University

School of Physics & Astronomy,

Department of Condensed Matter Physics

By

Yoni Erlich

August 2019

Under the supervision of Dr. Haim Suchowski

Abstract

Ultrashort laser pulses are in the heart of ultrafast phenomena research due to their short time scale, high peak power intensity, and broad spectrum. Ultrashort lasers can undergo second harmonic generation (SHG), which is one of the most basic and straightforward nonlinear processes. Ultrashort SHG, combines the high peak power of the ultrashort laser, with the simplicity of the SHG process, which is highly used in a variety of fields such as nonlinear spectroscopy, imaging for metallurgy, photo-induced dynamics and noninvasive background-free diagnostics. The need for ultrashort pulses and specifically ultrashort SHG, in various wavelengths and the fact that some wavelength regions are not easily accessible, have suggested the use of frequency conversion schemes. Most schemes usually require a tradeoff between the conversion efficiency and the bandwidth. In the past decade, a new scheme has emerged, the adiabatic frequency conversion, which can overcome the tradeoff between efficiency and bandwidth. However, it requires instead a long interaction length. In this thesis, we introduce a new scheme that is broad and efficient, which supplement the adiabatic scheme: by offering more solutions to overcome the efficiency bandwidth, it is less broad but requires much shorter interaction length. We experimentally demonstrate efficient SHG of tunable ultrashort pulses of 100 femtosecond, using novel method based on composite segmented periodically poled (CSPP) design. The scheme was borrowed from the nuclear magnetic resonance (NMR) composite pulses (CP). Using CSPP, a broadband and efficient conversion over a bandwidth of 35 nm in very short interaction length was achieved. Furthermore, we harnessed a novel numerical simulation, which was developed in our lab, to simulate the CSPP design in the ultrashort regime. The CSPP shows excellent robustness to temperature changes. The experimental results are compared to numerical simulation with an excellent agreement, and the CSPP performance show to be superior to periodically poled design in all aspects. This new scheme opens a new family of schemes - CP, for broad frequency conversion in a rather short interaction length.

Table of Contents

Acknowledgments

I wish to express my gratitude to my supervisor, Dr. Haim Suchowski, for his guidance and support during this project. I would like to express my appreciation to Dr. Andon rangelov for elaborating discussions on the theoretical aspects of this project. I would like to thank the femto-nano group, for their friendship and support.

List of Figures

List of Tables

1 Theoretical Backround

1.1 Introduction

Nonlinear optics is the science that investigates the nonlinear response of materials when they interact with light. Usually, nonlinear response refers to the nonlinear dependence of physical phenomena in the optics field strength [4]. In this chapter, I will briefly discuss the basics of Nonlinear optics (Sections 1.2-1.3), Ultrafast physics (section 1.4), Two level system (Section 1.5) and Geometric representation of two level system dynamics (Section 1.6). All will serve as a basis for the development of the CP in nonlinear optics.

1.2 Nonlinear processes with χ^2

When dealing with conventional light matter interaction, the linear relation between the polarization and the electric field is:

$$P(t) = \varepsilon_0 \chi^{(1)} E(t) \tag{1.1}$$

Where P is the polarization, ε_0 is the permittivity of free space, $\chi^{(1)}$ is the linear susceptibility, and E is the electric field. It is important to note that from convenience consideration, we are dealing with scalar terms, when, in fact, this is a vector equation and $\chi^{(1)}$ is a tensor. When dealing with strong fields, the above relation can be generalized as a power series:

$$p(t) = \varepsilon_0[\chi^{(1)}E(t) + \chi^{(2)}E^2(t) + \chi^{(3)}E^3(t) + ...] \tag{1.2}$$

Where $\chi^{(2)}$ and $\chi^{(3)}$ are the second and third-order nonlinear susceptibilities, respectively. Usually the higher term in the power series, the smaller it is comparing to lower terms, this is the reason that in order to view a nonlinear phenomena, a strong field is required. In our research, we will be dealing with the processes which relate to $\chi^{(2)}$, as illustrated in Fig.1.1 (a) and neglect higher terms. In order to get intuition about these processes, lets define the terms in the power series that relates to $\chi^{(2)}$ as second-order polarization: $p^{(2)}(t) = \varepsilon_0 \chi^{(2)} E(t)^2$. In later sections, we will show that the nonlinear terms of the polarization can act as a source for a generation of a new frequency component of the electric field.

1.2.1 *Second harmonic, sum and difference frequency generation*

Assume we have the following field $E(t) = E_1 e^{-i\omega_1 t} + E_2 e^{-i\omega_2 t}$, therefore, according to equation 1.2, the second order polarization will be:

$$p^{(2)}(t) = \varepsilon_0 \chi^{(2)} [E_1^2 e^{-2i\omega_1 t} + E_2^2 e^{-2i\omega_2 t} + 2E_1 E_2 e^{-i(\omega_1+\omega_2)t} + 2E_1 E_2^* e^{-i(\omega_1-\omega_2)t} + c.c] + 2\varepsilon_0 \chi^{(2)} (E_1 E_1^* + E_2^* E_2) \tag{1.3}$$

The polarization has serval frequencies components, which are different from the original field frequency. Each term, respectively, act as a source for the generation of the following processes: second harmonic generation-SHG $(2\omega_1, 2\omega_2)$, sum frequency generation - SFG $(\omega_1 + \omega_2)$ and different frequency generation - DFG $(\omega_1 - \omega_2)$. The DC term is called optical rectification. It is useful to look at these processes in an energy level scheme, as shown in Fig.1.1 (b)-(d). From those diagrams alone, we can learn an important difference between the processes. SFG and SHG are quite similar, as shown in Fig.1.1 (b) and (c), however, DFG is rather different. In the DFG process, as shown in Fig.1.1 (d), to create a new frequency, one photon, with the higher frequency must be destroyed, and the photon with the lower frequency must be created, resulting enhancement in the power of the electric field of the lower frequency. Along this chapter, we will use the following notation: in the case of two inputs fields, the strong field is named the pump, and the other is named the signal. The generated frequency is named idler.

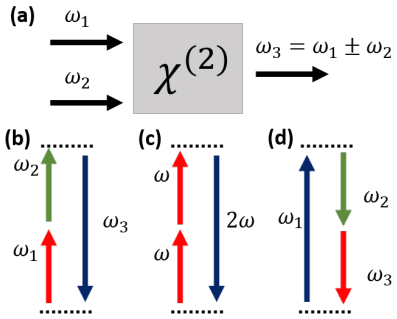

Figure 1.1: Schemes for nonlinear process via $\chi^{(2)}$. (a) The scheme of the system. (b) Energy scheme for SFG process. (c) Energy scheme for SHG process. (d) Energy scheme for DFG process.

1.3 Three wave mixing (TWM)

In this section, we will show, using the Maxwell equation, that the nonlinear polarization acts as a source, generating new frequencies. Without the loss of generality, we will deal with the SFG process. The physical picture, as shown in Fig.1.2 (a) is as follows: a strong input field, enters the

nonlinear material, and it has two frequencies components. Under the SFG process, the atoms will respond with an oscillating dipole moment. Due to nonlinearity, some of those dipoles moment oscillations frequency will be the sum of the two frequencies component. Naturally, the dipoles oscillate with different phases, preventing the generation of a strong field in the new frequency, this phenomena is often named as the phase mismatch problem [4]. However, there are methods to solve this problem, resulting in a well-defined field with the new frequency.

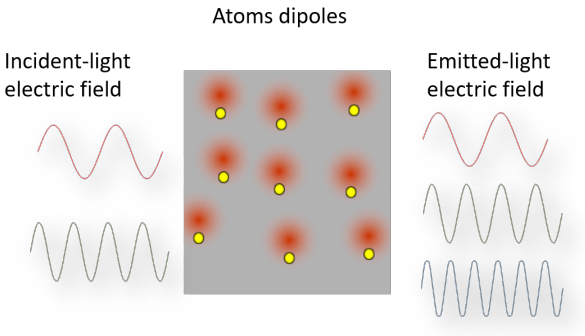

Figure 1.2: Schemes for the physical process of SFG. Atoms dipoles will respond with oscillations. Due to nonlinearty some of those dipoles moment oscillations frequency will be the sum of the two frequencies component. Taken from Professor Trebino lectures [1].

1.3.1 Derivation of the TWM equations

In appendix A, using the Maxwell equations, the wave equation for the nonlinear process is derived. This equation has the form of a driven wave equation. Where the source term is the nonlinear polarization. If the electric field and the polarization can be decomposed to the sum of plane waves, each with different frequency, the following equation will hold:

$$\nabla^2 E_n(\mathbf{r}) + \frac{\varepsilon^{(1)}\omega_n^2}{c^2}\frac{\partial^2}{\partial t^2}E_n(\mathbf{r}) = -\frac{\omega_n^2}{\varepsilon_0 c^2}\frac{\partial^2}{\partial t^2}(P_n^{NL}(\mathbf{r})) \tag{1.4}$$

Assuming $E(t) = E_1 e^{-i\omega_1 t} + E_2 e^{-i\omega_2 t}$, than if it enters a material and goes through SFG process, a new frequency will be generated $\omega_3 = \omega_1 + \omega_2$. As mention before, we will decompose the electric field and the polarization into their frequency component: $E_j(z,t) = E_j e^{-iw_j t} + c.c$ where $E_j = A_j e^{+ik_j t}$. We assumed slowing varying amplitude of the electric field and that the spatial dependence is only on the optical axis z. We will derive the wave equation for the generated frequency. According to equation 1.2 and 1.3, the amplitude of the polarization in this frequency will be: $P_3 = 2\varepsilon_0 A_1 A_2 e^{i(k_1+k_2)}$. By inserting the term of ω_3 into equation 1.4 and assuming slowly varying amplitude - $|\frac{d^2A_3}{dz^2}| << |k_3\frac{dA_3}{dz}|$, the equation for ω_3 takes the form:

$$\frac{dA_3}{dz} = \frac{i\chi^{(2)}\omega_3^2}{k_3c^2}A_1A_2e^{i\Delta kz} \tag{1.5}$$

where $\Delta k = k_1 + k_2 - k_3$,which is called the wavevector mismatch. We will see in later sections that this term plays important role in frequency conversion. In the same manner the equation for the two other frequencies can be derived:

$$\frac{dA_1}{dz} = \frac{i\chi^{(2)}\omega_1^2}{k_1c^2}A_2^*A_3e^{-i\Delta kz} \tag{1.6}$$

$$\frac{dA_2}{dz} = \frac{i\chi^{(2)}\omega_2^2}{k_2c^2}A_1^*A_3e^{-i\Delta kz} \tag{1.7}$$

1.3.2 The phase matching problem- an observation in the undepleted regime

The physical meaning of wavevector mismatch is that there is a phase between different atomic dipoles, resulting in a destructive contribution to the generated beam. If there is no mismatch, then all the dipoles are in phase thus they will add up, resulting generation of a new frequency term. Even in the case of zero mismatch, the energy flow can oscillate between the new frequency and the input fields signal frequency. This is called back conversion. To understand this more intuitively, let's deal with the most simple case, where both the input fields are undepleted. If $\Delta k = 0$, meaning perfect phase matching, then, after integrating equation 1.5, the amplitude of the sum frequency will grow linearly with the interaction length: L and the intensity will grow with its square, $I_3 \sim L^2$ [4]. However, in the case Δk non zero, the generated intensity will be [4]:

$$I_3 = \frac{2\chi^{(2)2}\omega_3^2 I_1 I_2}{n_1 n_2 n_3 \varepsilon_o c^2} L^2 sinc(\frac{\Delta kL}{2}) \tag{1.8}$$

Where L is the interaction length, I_i is the intensity of the fields, and n_i is the index of refraction for the i'th frequency. We can see that the sinc term is the result of phase mismatch. In addition, the intensity of the generated field decreases with the increase of the term ΔkL. Therefore, one can define the coherence length- the length in which above it, the generated wave is out of phase: $L_{coherence} = \frac{\pi}{\Delta k}$. The sinc function is plotted in Fig.1.3 (a). We can learn that the deviation from zero phase matching results in a major decrease in the efficiency of the SFG process.

In the case of SHG process one equation becomes redundant since $A_1 = A_2$, resulting:

$$\frac{dA_1}{dz} = \frac{i\chi^{(2)}\omega_1^2}{k_1c^2}A_1^*A_3e^{-i\Delta kz} \tag{1.9}$$

$$\frac{dA_3}{dz} = \frac{i\chi^{(2)}\omega_3^2}{k_3c^2}A_1^2e^{i\Delta kz} \tag{1.10}$$

And if we assume again undepleted inputs and Δk non zero, the SHG intensity will take the following form:

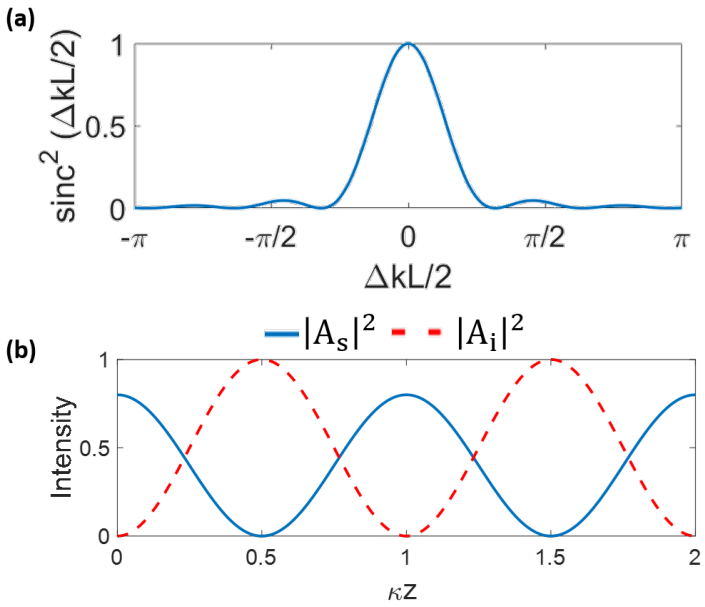

Figure 1.3: (a) Sinc function, representing the conversion efficiency of the SFG process in the case of undepleted pump and signal. (b) Back conversion between the signal and the idler in the case of perfect phase matching in the undepleted pump regime.

$$I_3 = \frac{\chi^{(2)2}\omega_3^2 I_1^2}{n_1^2 \varepsilon_o c^2} L^2 sinc(\frac{\Delta kL}{2}) \tag{1.11}$$

We can see that there is a factor $\frac{1}{2}$ for the SHG. This is expected because there is only one signal that enters the crystal. It is essential to note the SHG process sensitivity to the input intensity - it grows with the square of the inserted beam intensity, which is referred to as the pump.

It is worth noting that in the case of the undepleted pump, where the signal can change, the intensity of the generated frequency - the idler, will go like $sin^2[\sqrt{(\frac{1}{4}\Delta k^2 + \kappa^2)}z]$ where $\kappa = \frac{2\chi^{(2)}\sqrt{k_1 k_3}}{n_1 n_3} A_2$. From this, we can learn that even in the case of zero phase matching, the efficiency of the process can be decreased, due to back conversion, where the idler is converted back to the signal, as illustrated in Fig.1.3 (b). In fact, as we will see later on, this kind of behavior resembles a two level system.

1.3.3 Solving the phase matching problem

There are many methods that deal with the phase matching problem [4, 5, 6, 7, 8, 9]. We will discuss the Quasi Phase Matching (QPM) technique which is one of the most common. When we write $\chi^{(2)}$, we relate to the effective $\chi^{(2)}$ that couples the interacting waves. The QPM technique

changes the sign of the effective $\chi^{(2)}$, in a periodical fashion, as shown in Fig.1.4 (b). The periodic alternation of the second order nonlinear susceptibility can compensate for the phase mismatch.

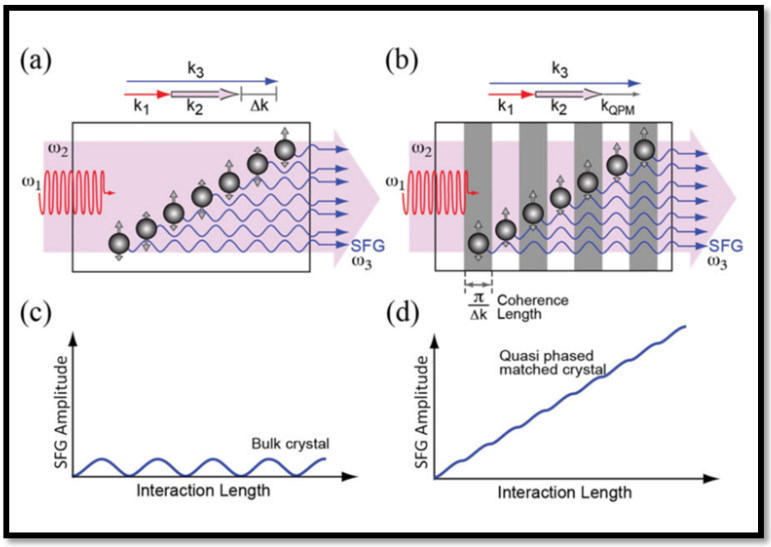

Figure 1.4: (a) Non-phase matched interaction (b) Quasi phased-matched interaction (c) The generated SFG intensity for the nonphase matched case. (d) The generated SFG intensity for QPM interaction. Taken from Ref. [2].

Assuming the sign alternation is with period Λ, then, the effective $\chi^{(2)}$ can be written as:

$$\chi^{(2)}(z) = \chi^{(2)}_{eff} sign[cos(2\pi z/\Lambda)] \tag{1.12}$$

Since it is a periodic function, it can be described as a Fourier series:

$$\chi^{(2)}(z) = \chi^{(2)}_{eff} \sum G_m e^{ik_m z} \tag{1.13}$$

Where $k_m = \frac{2\pi m}{\Lambda}$ and $G_m = \frac{2sin(m\pi/2)}{m\pi}$. If we assume that the first term, m=1, is the dominant and neglect higher terms, then, the TWM equations get the following approximation:

$$\frac{dA_3}{dz} = G_1 \frac{i\chi^{(2)}_{eff}\omega_3^2}{k_3 c^2} A_1 A_2 e^{iz(\Delta k - 2\pi/\Lambda)} \tag{1.14}$$

$$\frac{dA_1}{dz} = G_1 \frac{i\chi^{(2)}_{eff}\omega_1^2}{k_1 c^2} A_2^* A_3 e^{-iz(\Delta k - 2\pi/\Lambda)} \tag{1.15}$$

$$\frac{dA_2}{dz} = G_1 \frac{i\chi^{(2)}_{eff}\omega_2^2}{k_2 c^2} A_1^* A_3 e^{-iz(\Delta k - 2\pi/\Lambda)} \tag{1.16}$$

Therefore, if the period of the alternation is chosen in the following manner: $\Lambda = \frac{2\pi}{\Delta k}$, the phase mismatch could be compensated as shown in Fig.1.4 (b) and (d). It is important to note, that since this is an approximation - taking the first term of the Fourier series, the efficiency of the QPM will not be as high as with perfect phase matching. Another important comment that will be discussed later on is the fact that QPM only solve the phase matching problem for a single frequency. Therefore, this method will not be able to efficiently convert an ultrashort laser pulse, since it is inherently with a broadband spectrum.

1.3.4 The Adiabatic scheme- broad and efficient frequency conversion

One can argue that in order to achieve broad frequency conversion, the period of the polling of the crystal, needs to be changed along with the crystal, to fit all the input bandwidth: $\Lambda = \Lambda(z)$. However, by doing this alone, broad bandwidth conversion could be achieved, but with poor efficiency. In the past decade, a new method has emerged - the adiabatic scheme, a method that allows to overcome the tradeoff between conversion efficiency and bandwidth.

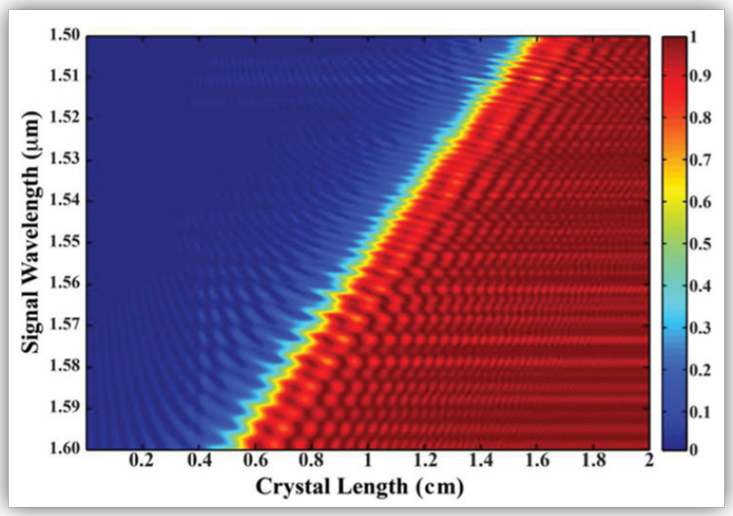

Figure 1.5: Adiabatic conversion for SFG process for adiabatic aperiodic design along the propagation axis (horizontal axis) and different input wavelength (vertical axis). Taken form Ref. [2]

The adiabatic evolution is a dynamical process for classical and quantum systems, which allows a robust way of changing a system into the desired state [10, 11]. Suchwoski et al. [2, 5] found that by implementing the adiabatic evolution into the realm of nonlinear optics, broad and efficient frequency conversion can be achieved for SFG, DFG, and SHG processes. This can be achieved if the change of the period along the crystal is slow enough, which means that:

$$|\frac{\Delta k}{dz}| << \frac{(\Delta k^2+\kappa^2)^{3/2}}{\kappa} \tag{1.17}$$

where $\kappa = \frac{2\chi^{(2)}\sqrt{k_1 k_3}}{n_1 n_3} A_2$, a broad and efficient conversion can be achieve without back conversion, as shown in Fig.1.5. Also, the scheme has a high robustness to variations in the parameters of both the nonlinear crystal and of the incoming light. We will define the crystal grating function in the following manner: $K_g(z) = \frac{\pi}{\Lambda(z)}$. Thus, the second order nonlinear susceptibility is:

$$\chi^{(2)}(z) = \chi^{(2)}_{eff} sign[cos(zK_g(z)] \tag{1.18}$$

therefore, $\chi^{(2)}$ will fluctuate between $+\chi^{(2)}$ $-\chi^{(2)}$, in spanning batches. As shown in Fig.1.5, each frequency is generated in a different location along with the crystal, where $\Delta k(\omega_i) = 0$. Thus, there is an inherent demand, requiring longer crystal for broader and efficient conversion. Our new method, which will be presented later on, supplement the adiabatic scheme, using short crystal length, in regimes where not a very broad bandwidth is required.

1.4 Ultrashort regime

In this section, we will briefly discuss the added consideration for frequency conversion when one deals with ultrashort pulses and our novel time domain simulation for the ultrashort regime. Ultrashort pulses have a spanning time scale of femtosecond, which is 10^{-15} second. While continues wave (CW) laser emits a specific wavelength continuously, an ultrashort laser emits many wavelengths in a short time. As shown in Fig.1.6 (a), in the time domain ultrashort pulse is rather short, and CW is long, but in the frequency domain, the short pulse has a broad bandwidth.

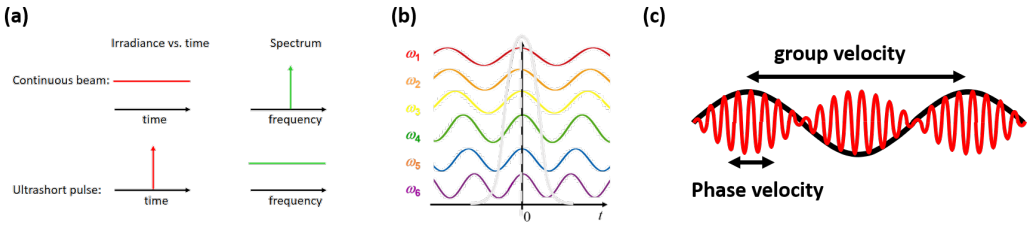

Figure 1.6: (a) Illustration of the fundamental difference between CW and ultrashort pulse. (b) Illustration of generation of ultrashort pulse. (c) Illustration of the difference between group velocity and phase velocity. Taken from Professor Trebino lectures [1].

The major difference between an ultrashort laser and other sources that emit a broadband spectrum (like a light bulb), is the fact that in some specific time, there will be phase coherence between different frequencies for the ultrashort pulse, as illustrated in Fig.1.6 (b).

An important feature of an ultrashort pulse is its peak intensity. The average pulse power can be rather low. However, due to its short time scale, during a short time, there is a significant peak in the intensity, as shown in Fig.1.6 (b). The peak power can be calculated in the following manner:

$$I_{peak} = \frac{P_{ave}}{Sr\tau} \tag{1.19}$$

Where S is the beam area, r is the repetition rate, τ is the pulse length and P_{ave} is the average power. We saw in previous sections that the efficiency of SHG grows with the square of the incoming beam intensity, hence, due to high peak intensity, ultrashort pulses are in the heart of nonlinear interaction.

When dealing with frequency conversion of ultrashort pulses, the influence of higher dispersion terms becomes very relevant. When assuming planar waves and that the pulse bandwidth is much smaller than its central frequency, the phase can be express as a Taylor series:

$$k(\omega)L = k(\omega_0)L + k'(\omega_0)[\omega - \omega_0]L + k''(\omega_0)[\omega - \omega_0]^2 L + ... \tag{1.20}$$

1.4.1 Group velocity mismatch (GVM)

The GVM is the result of the second term of equation 1.20. The group velocity, which is illustrated in Fig.1.6 (c), is defined as follows:

$$v_g = \frac{d\omega}{dk} \tag{1.21}$$

Different frequencies shall have different group velocity. This effect decreases the nonlinear efficiency process and effectively makes the interaction length shorter between different pulses. For example, SHG efficiency can suffer from this effect, due to the difference of the group velocity, the SHG will lag after the pump, as illustrated in Fig.1.7. This can result in destructive interference between the generated SHG pulses. Also, this effect can cause the SHG pulse length to increase. The GVM is defined as:

$$GVM = \frac{1}{v_{g1}} - \frac{1}{v_{g2}} \tag{1.22}$$

where v_{g1}, v_{g2} are respectively the signal and the idler pulses or the SH and its pump. We can estimate the propagation length, in which the two pulses will still overlap: $L_{QS} = \tau / GVM$. This length can help us to understand if the system is in the ultrashort regime. For example, in the SHG process for 100 fs pump at 1030 nm on Mg-doped $LiNbO_3$: $L_{QS} \sim 0.3mm$, this means that for interaction beyond this length, the conventional TWM equations should by alter to equations 1.24-26, which will be introduced later on. To limit the effect, the crystal length should be smaller than L_{QS}. Therefore, long crystals will suffer from group mismatch velocity.

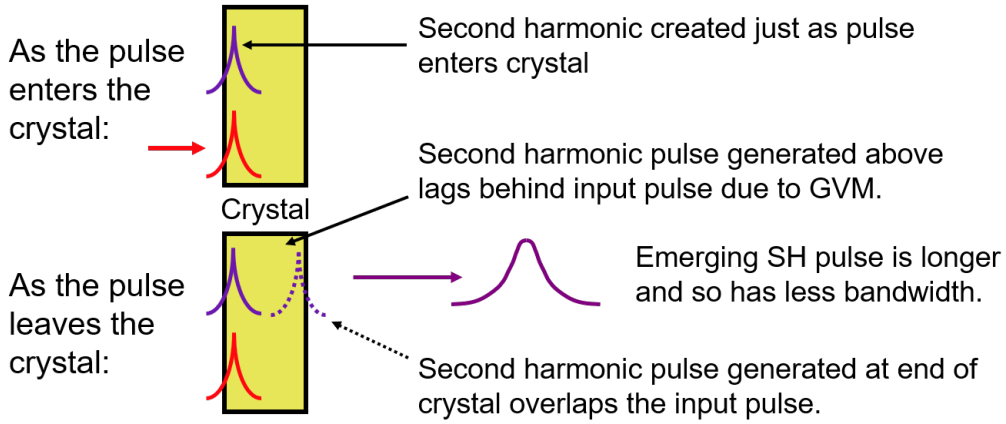

Figure 1.7: Illustration of the how GVM effects the SHG process. Taken from Professor Trebino lectures [1].

1.4.2 Group velocity dispersion (GVD)

GVD, is the result of the third term of equation 1.20. It is defined as

$$GVD = \frac{d^2\omega}{d^2k} \tag{1.23}$$

GVD causes to the temporal spreading of the pulse. Again we can define a propagation length on which the spreading is of the same order of the pulse length: $L_{GVD} = \tau^2/GVD$. For a pulse centered around 1030 nm, with FWHM of the order of 100fs, this phenomena can be neglected, however, in the order of 1fs, this phenomena is highly relevant: $L_{GVD}(100fs) = 556mm, L_{GVD}(1fs) = 0.05mm$, where the medium is on Mg-doped $LiNbO_3$. In our experiment, we work with pulses at 100 fs. Therefore this phenomena is not relevant for our analysis.

1.4.3 Novel numerical simulation- generalization of the frequency conversion processes to the ultrashort regime

In our lab, Dahan et al. [12] have developed a framework to simulate nonlinear TWM processes in the ultrashort regime, allowing an analysis of any three waves mixing with arbitrary phase mismatched design.

When going beyond the monochromatic regime, the TWM takes the following form in the time domain:

$$\frac{\partial B_1(z,t)}{\partial z} + iF^{-1}(\beta(\omega+\omega_1)B_1(z,\omega)) = -i\frac{\chi^{(2)}(z)\omega_1}{cn_1}B_3B_2^* \tag{1.24}$$

$$\frac{\partial B_2(z,t)}{\partial z} + iF^{-1}(\beta(\omega+\omega_2)B_2(z,\omega)) = -i\frac{\chi^{(2)}(z)\omega_2}{cn_2}B_3B_1^* \tag{1.25}$$

$$\frac{\partial B_3(z,t)}{\partial z} + iF^-1(\beta(\omega+\omega_3)B_3(z,\omega)) = -i\frac{\chi^{(2)}(z)\omega_3}{cn_3}B_1B_1 \tag{1.26}$$

Where $B_i(z,\omega) = A_i(z,\omega)e^{\frac{i\omega n(\omega_1)}{c}}$ and we assumed that the electric field is planar. Moreover, the analysis takes under account four wave mixing (parasitic) effects of two photon absorption (TPA) and Kerr effect for all involving waves. According to Ref. [4], when the nonlinear medium experiences TPA, an intensity dependent term is added to the linear absorption constituting an absorption coefficient:

$$\alpha = \alpha_o + \gamma I \tag{1.27}$$

Therefore, in the simulation, the following term is added: $-\frac{1}{2}\gamma I_{SHG}B_{SHG}$ to the SHG differential equation. For a full analysis, see Ref. [12]. The numerical simulations of the equations above are performed by implementing the split-step Fourier method for the linear part of the equations, while the numerical integration for the nonlinear part is implemented using the 4th order Runge–Kutta method. It is important to note that the simulation assumes plane waves. Moreover, it was demonstrated that for adiabatic SHG, the simulation results are in a very good agreement with SHG experiment measurements [13].

1.5 Two level system

Two level system model plays an essential rule in exploring the dynamical nature of many physical systems in various fields, including NMR, light-matter interaction, and frequency conversion. Moreover, to later understand the composite pulse schemes, which are the basis of the thesis, one should be familiar with two level system notation. A two level system can be described as an atom with two energy levels, an electron in a potential well or 1/2 spin [14]. For convenience, we will discuss a two-level system through the atomic point of view, as shown in Fig.1.8.

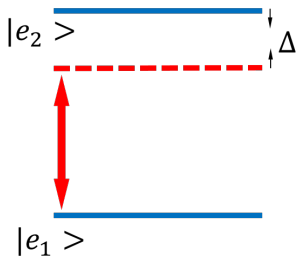

Figure 1.8: Illustration of two level system. The parameters Ω_R and Δ are the physical parameters that describe the dynamics of the system and will be discuss in the text.

In the presence of an electric field of the form: $E = E_0 cos(\omega t + \phi)$, the Hamiltonian, under the rotating wave approximation, becomes time dependent in the following way [14]:

$$H(t) = \varepsilon_1 \hat{N}_1 + \varepsilon_2 \hat{N}_2 - \frac{\hbar\Omega_R}{2}[e^{i\omega t + i\phi}\hat{\sigma_-} + e^{-i\omega t - i\phi}\hat{\sigma_+}] \tag{1.28}$$

Where we defined: $\hat{N}_1 = |e_1><e_1|, \hat{N}_2 = |e_2><e_2|$, $\hat{\sigma_-} = |e_1><e_2|, \hat{\sigma_+} = |e_2><e_1|$ and $\Omega_R = qE < e_1|r|e_2 >$. See full analysis in appendix B.

In order to solve the Schrodinger equation: $i\hbar\frac{d|\psi(t)>}{dt} = \hat{H}|\psi(t)>$, we will assume the following form of solution:

$$|\psi(t)> = c_1(t)e^{-i\frac{\varepsilon_1 t}{\hbar}}|e_1> + c_2(t)e^{-i\frac{\varepsilon_2 t}{\hbar}}|e_2> \tag{1.29}$$

applying this Hamiltonian from the above equation, the equations for the coefficients are:

$$\frac{dc_1(t)}{dt} = i\frac{\Omega_R}{2}c_2(t)e^{-i\frac{\Delta t}{\hbar}+i\phi} \tag{1.30}$$

$$\frac{dc_2(t)}{dt} = i\frac{\Omega_R}{2}c_1(t)e^{+i\frac{\Delta t}{\hbar}-i\phi} \tag{1.31}$$

where $\Omega = \sqrt{\Omega_R^2 + (\Delta/\hbar)}$ and the detuning, Δ is defined as: $\Delta = \varepsilon_2 - (\varepsilon_1 + \hbar\omega)$. Solving the two coupled equations, under the assumption that the system is initially in the ground state, we get the following [14]:

$$c_1(t) = e^{-i\frac{\Delta t}{2\hbar}}[cos(\frac{\Omega t}{2}) + i\frac{\Delta}{\Omega\hbar}sin(\frac{\Omega t}{2})] \tag{1.32}$$

$$c_2(t) = e^{i\frac{\Delta t-\phi}{2\hbar}}[i\frac{\Omega_R}{\Omega}sin(\frac{\Omega t}{2})] \tag{1.33}$$

From this solution, we can learn the physical meaning of the detuning and Ω_R, as shown in Fig.1.9. If the detuning is zero, the probabilities, for being in the exited and the ground state will oscillate between 0 and 1, respectively, with frequency equals Ω_R , generating complete population transfer between the two states, as illustrated in Fig.1.9 (a) and (b). However, in the presence of detuning, the population will oscillate with frequency Ω, and there will be no complete population transfer, as illustrated in Fig.1.9 (c) and (d). Also, as Ω_R or Δ is increased, so does the probabilities oscillations. To conclude, in two level system, there are two terms which are responsible for the dynamics. The detuning will affect the maximum population difference [14]: $|c_2(t)|^2 - |c_1(t)|^2 = \frac{\Omega_R^2 - (\Delta/\hbar)^2}{\Omega_R^2 + (\Delta/\hbar)^2}$ and Ω_R will affect the strength of the oscillations.

1.5.1 Analogy between TWM and two level system

We showed that the SFG and DFG are described by the TWM equations that were introduced in earlier sections. The TWM equations can be reduce to two coupled equations, if we assume that

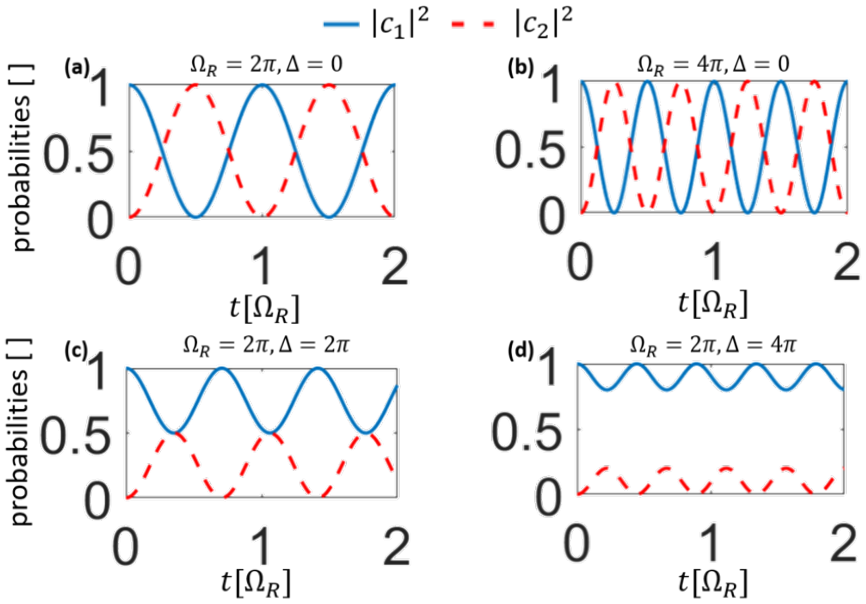

Figure 1.9: Illustration of the two level dynamics. (a) The probabilities in the ground state and the excited state under no detuning. (b) Similar to (a) with a higher Ω_R, the population transfer frequency is increased. (c) The probabilities in the ground state and the excited state with detuning. (d) Similar to (c) with a higher Δ, the population transfer frequency is increased.

one of the inserted waves (the "pump") is constant - this is called the undepleted pump regime. Applying $A_2 = const$ to equations 1.5-1.7, we get [2]:

$$\frac{da_1(z)}{dz} = a_3 i \frac{\chi^{(2)}\omega_1\omega_3}{\sqrt{k_1 k_2 c^2}} A_2 e^{-i\Delta k z} \tag{1.34}$$

$$\frac{da_2(z)}{dz} = a_1 i \frac{\chi^{(2)}\omega_1\omega_3}{\sqrt{k_1 k_2 c^2}} A_2 e^{i\Delta k z} \tag{1.35}$$

where $a_1 = \frac{\sqrt{(k_1)}}{\omega_1 A_2} A_1$ and $a_3 = \frac{\sqrt{(k_3)}}{\omega_3 A_2} A_3$. Now if we observe the coupled equations: 1.32 and 1.33, for two level system, we can see that the SFG and DFG processes in the undepelted pump regime, behave as a two level system where Ω_R is analog to $\frac{\chi^{(2)}\omega_1\omega_3}{\sqrt{k_1 k_3 c^2}} A_2$ and the detuning Δ is analog to Δk. For convenience we will define: $\kappa = \frac{\chi^{(2)}\omega_1\omega_3}{\sqrt{k_1 k_3 c^2}}$.

This analogy suggests to use schemes from other fields of physics into nonlinear optics (see Ref [2]). In nonlinear optics, full population transfer will mean that all the photons from the signal were converted to photons of the new frequency, the idler. In this research, we apply CP schemes of Shaka and Pine to nonlinear optics, which was theoretically suggested by Rangelov et al. [15].

1.6 Geometric representation of two level dynamics - Bloch sphere

The two level dynamics can be geometrically described in a Bloch sphere [16, 17]. This approach can give intuition and broader understanding of the two level dynamics, which in turn will enable a better understanding of the effects of spatially varying coupling and phase mismatch [18].

We will use the density operator approach in the Schrodinger picture:

$$i\frac{d\hat{\rho}}{dt} = [\hat{H(t)}, \hat{\rho}] \tag{1.36}$$

where $\hat{\rho}$ is a 2×2 matrix and H is the Hamiltonian as was describe in equation 1.28. By using this approach, the dynamics can be describe in a single vector equation [16, 17]:

$$\frac{d\vec{V}(t)}{dt} = \Omega \times \vec{V}(t) \tag{1.37}$$

where we defined:

$$V_x = \rho_{21}(t)e^{i\omega t + i\phi} + \rho_{12}(t)e^{-i\omega t - i\phi} \tag{1.38}$$

$$V_z = \rho_{22}(t) - \rho_{11}(t) \tag{1.39}$$

$$\vec{\Omega} = -\Omega_R\hat{x} + \Delta/\hbar\hat{z} \tag{1.40}$$

These equations have important properties. First, when no losses occur, the magnitude of $\vec{V}(t)$ is constant, this means that the dynamics are on a sphere with radius $|\vec{V}|$, as illustrated in Fig.1.10 (a). Second, the vector V is under periodic motion, where the frequency is $|\vec{\Omega}|$. Third, the vector $\vec{\Omega}$ is always normal the plane of rotation, as shown in Fig.1.10 (b). The plane of rotation is the plane in which the tip of the vector V lies during its rotation.

1.6.1 Visualization of two level dynamics

By observing V_z in equation 1.39, we learn that it describes the population difference between the two states. Therefore, since the magnitude of V is constant, if the vector V is on $-\hat{z}$ direction, it means that the system is in the ground state. Then, If V goes through some trajectory, where it ends with pointing to $+\hat{z}$, it means that there was a complete population transfer, from the ground state to the excited state.

Let's assume that the initial state is V $=-\hat{z}$. In the case of zero detunings: $\vec{\Omega} = -\Omega_R\hat{x}$, this means that $\vec{V}$ will rotate with frequency Ω_R in the y-z plane since x will be the axis of rotation, as shown in Fig.1.10 (b). We can see, that at times that satisfy: $\Omega_R t = \frac{\pi}{2}$, V will go from one pole to the other, allowing full population transfer. This phenomenon is called Rabi flopping.

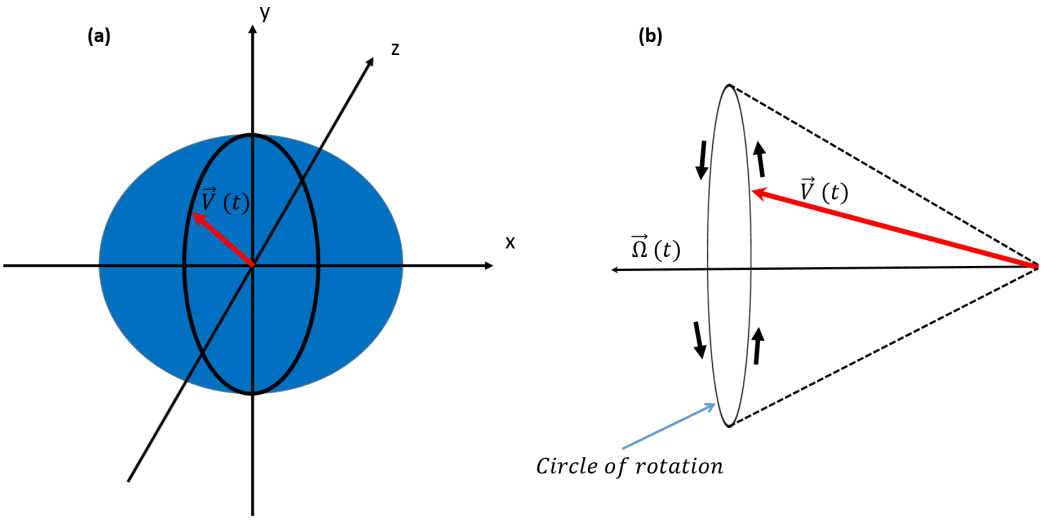

Figure 1.10: Geometrical representation of two level system on a Bloch sphere. (a) The vector V has a constant magnitude and therefore its tip always lies on the sphere. (b) The vector V rotates in a plane which is perpendicular to Ω.

However, in the case of non zero detuning, Ω will take the following form: $\vec{\Omega} = -\Omega_R\hat{x} + \frac{\Delta}{\hbar}\hat{z}$. This means that the axis of rotation will not be on the y-z plane, as illustrates in Fig.1.11. Therefore, as V rotates, it will never reach the north pole - preventing full population transfer. Moreover, as the detuning increase, the plane of rotation tilts in a manner that reduces its radius, causing a decrease in the population transfer, as shown in Fig.1.11.

To summary, if we visualize the dynamics of two level system on the Bloch sphere, the following holds: the vector V, which its z component represents the population difference, does not change its magnitude. Therefore the dynamics in the geometric representation will be a trajectory on the Bloch sphere. The vector $\vec{\Omega}$ represents the axis of rotation and its magnitude the frequency of rotation. In the case of zero detunings, for a specific time, full population transfer is possible. For non zero detunings, there will never be a full population transfer. The vector V will oscillate in a trajectory of a circle, where its radius will decrease with the increase of the detuning.

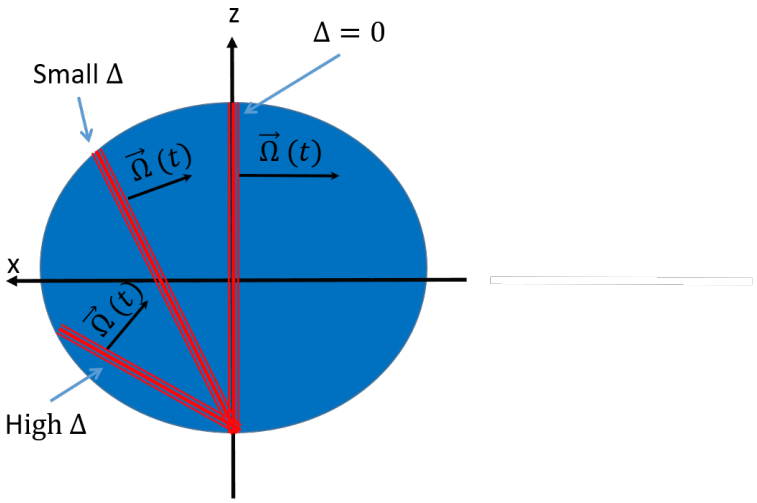

Figure 1.11: The effect of the detuning on the plane of rotation. As the detuning increased, the radius of the circles of rotation, in which V rotates, decreased. This effect reduces the population transfer.

2 Composite pulses

2.1 Introduction

Composite pulses (CP) were originated in the field of NMR [19], where it was used for spin population transfer. In the notation of NMR, CP, are rf sequences which can be parameterized according to their time duration and phase. NMR spectroscopy requires a precise rf pulse to allow spin population transfer. Therefore, to dismiss the need for a perfect system and exact excitation pulse, the CP was used. The CP has an inbuilt mechanism that allows robustness to experimental and pulse imperfections [19]. The CP can compensate for pulse shape errors, pulse duration errors, amplitude errors, and for spin-spin interactions, as shown in Fig.2.1. One of the first pioneers in the CP schemes is Levitt's widely used inversion schemes [19]. Levitt's demonstrated that a CP comprised of three pulses can enable a two-level spin j = $\frac{1}{2}$ system to undergo complete population transfer (CPT), with robustness to the pulse or system's imperfections. This schemes have since opened a wide variety of different composite pulse sequences, which revolutionized the field of NMR and its applications. Furthermore, in the case of NMR, CP sequence can allow to control and manipulate the direction of the electron spin and even flip spins with different orientation into the same orientation, which is analog to overcoming the phase mismatch problem, or in another word, to efficiently generate new frequencies from a broadband source.

In the following, we will elaborate on relevant notation related to composite pulses. A single CP pulse can be written as follows: 180_0. This can be understood via the geometrical approach that was presented in section 1.6. If we consider spin, the south pole of the Bloch sphere represents spin down, and the north pole represents spin up. The first term - 180 refer to the pulse time duration, given Ω, the pulse duration τ will be such that the spin will change its orientation in 180^0 on the Bloch sphere: $\Omega\tau = \pi$. The term 0 refers to the orientation of the vector Ω on the Bloch sphere, or from another point of view - the coupling coefficient phase. For example, we can define a Cartesian coordinate system over the Bloch sphere, as shown in Fig.2.2, there $\Omega = |\Omega|\hat{x}$. As we can see, the CP sequence is design for specific Ω. Therefore, if the actually Ω is different or the initial state of the spin is not down, the pulse 180_0 will not flip the spin, as shown in Fig.2.2 (b).

We can look at this problem from the following perspective: there is a group of spins, some

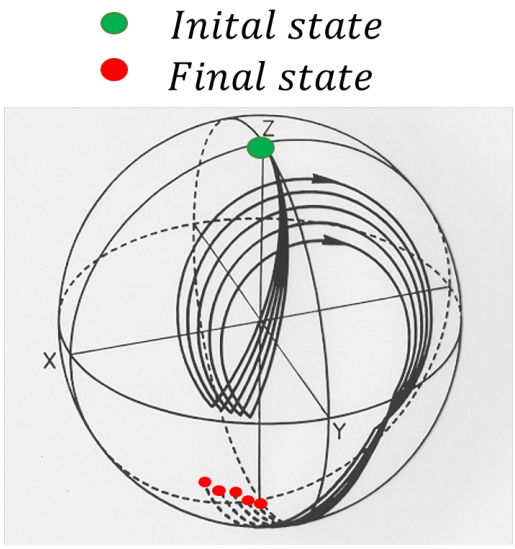

Figure 2.1: Example of the effect of CP pulse on an imperfect system. The dynamics are illustrated in a Bloch sphere. Five trajectories are shown, each corresponds to different detuning.

have the specific Ω that our CP is suited for, but others do not, thus, if we will activate the single pulse, only a few of the spin will flip. From a nonlinear perspective, the single pulse resembles the QPM periodic technique.

Lets observe the following CP pulse: $240_0 60_{180}$. We assume that one of the spins has detuning resulting in a lag of x degrees, since the Ω that we are using is for zero detuned spins, as illustrated in Fig.2.3. These two sequences compensate for the lag, resulting flip of both detuned and not detuned spins. However, in this analysis, we assumed that the plane of rotation would be perpendicular to Ω_R, this is not the case for the detuned spins. The detuned spins will rotate according to different Ω. Therefore they will deviate from a full flip. The approximation will be less accurate as the detuning will increased. This example was given as an intuition for why one would consider using such CP pulse, as we will see in the following section, under optimization, this kind of CP pulses can generate broad spin flip.

There are many types for CP sequences, and there is an entire field that discusses how, by optimization, one can generate CP sequences that will work for a large detuning. The CP technique relates to the propagator of the time-dependent Schrödinger equation for two states. The methods, which are beyond our scope, decompose the propagator U into a multiple of propagators:

$$U^{(N)}(A) = U_N(A_N(\delta t_N, \Omega_N))U_{N-1}(A_{N-1}(\delta t_{N-1}, \Omega_{N-1}))...U_1(A_1(\delta t_1, \Omega_1)) \tag{2.1}$$

Where $A = \int \Omega(t) \cdot t$. Then in order to find the CP, $U^{(N)}(A)$ is expand as a Taylor series around A=π for complete population transfer, then, by demanding form the set - $[t_i, \Omega_i]$ to nullify the

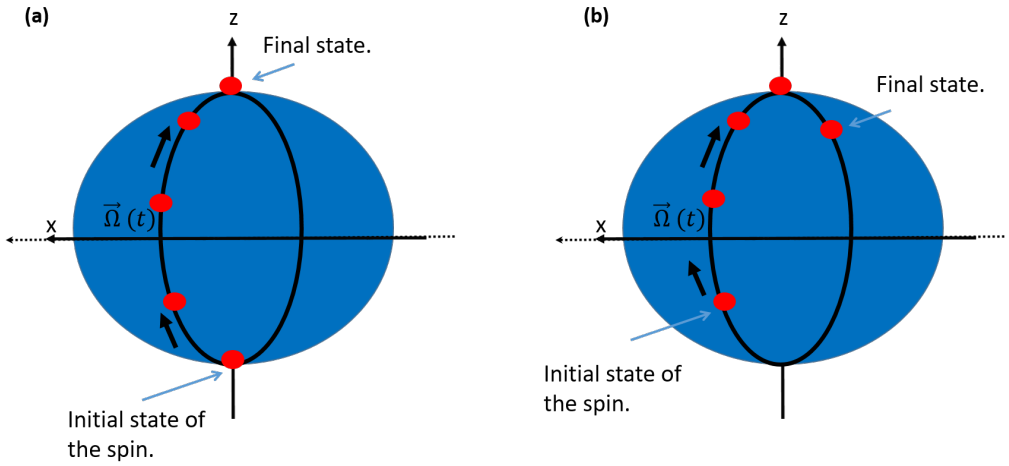

Figure 2.2: Example of the effect of a pulse 180_0. (a) If the spin is in the right orientation and the time duration of the pulse- π/Ω are correct, the pulse will flip the spin. (b) If the spin is not in the right orientation or the time duration of the pulse- π/Ω is not correct, the pulse will not flip the spin.

derivatives: $\frac{\partial^k}{\partial \delta^k} U^{(N)} = 0$ and $|U_{21}^{(N)}(\pi)| = 1$, the CP sequence that generate broad population transfer is derived [20].

2.2 The composite sequences of Shaka and Pines

In 1985 Shaka and Pines publish a letter discussing a new family of sequences of CP [3, 21]. They had an intuition that pulses of the form: $240_0 60_{180}$, where the orientation of Ω is bound to flip between 0 and 180: $\Omega = \pm|\Omega|\hat{x}$ can lead under optimization, to a full population transfer of detuned spins. They used non-linear optimization of the maximum detuning that can still allow full population transfer as function of the sequences time length [3], for example: $34.2_0, 123.0_{180} 197_0 288.8_{180}$. The important difference of these pulses from the pulses mentioned earlier is the fact that Shaka and Pines took under consideration the fact that the detuned spins will rotate around different planes. One can see that the total sum in degrees of the sequence is about 180, which means that nondetuned spins will flip. The change of the sign of the coupling - Ω, compensates for the detuned spins. The more the sequences that are applied, the more deviation is allowed - meaning increased in the bandwidth.

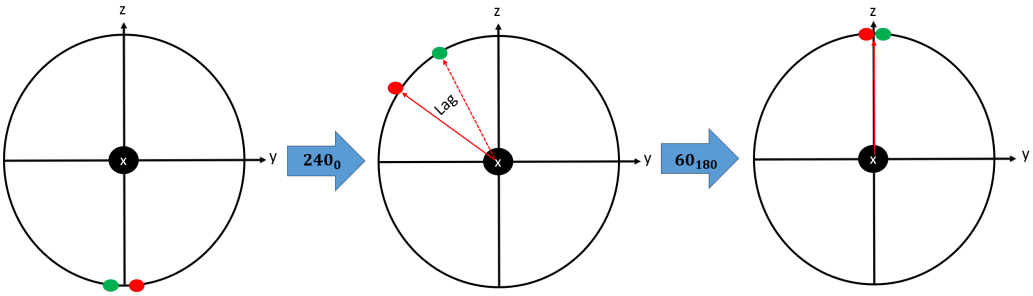

Figure 2.3: Example of CP - $240_0 60_{180}$, this kind of pulses can flip spins that have a lag. However, this is only true in the case of small detuning. Under high detuning the plane of rotation will deviate significantly, and the detuned spins will rotate according to a different Ω.

3 CP schemes in nonlinear optics

3.1 Implementation of CP schemes to nonlinear crystal

In this section, we will describe how to design a nonlinear crystal, suited to generate broad and efficient frequency conversion, based on the CP of Shaka and Pines.

First, we need to exploit the analogy further, we have mentioned that the detuning, Δ, is analog to Δk and Ω_R is analog to κ. Also, we note that the optical axis coordinate z is analog to the duration of the pulse. The pulse 180_0 means the following in nonlinear optics term : $\Omega_R = +|\kappa|$ and the length $z = \frac{\pi}{\kappa}$. Each segment of the sequence is referred to a nondetuned spin, or in our case, to the central frequency of the ultrashort pulse. Hence, $\chi^{(2)}$ will be periodical change in the manner discussed in section 1.3.3, in respect to the central frequency. Now if we wish to add another segment, 90_{180}, the length of this sequence will be $z = \frac{\pi}{2\kappa}$ and $\chi^{(2)}$ will still flip in the same period. However, now Ω_R changes it's sign, resulting change in the flip order: $+\chi^{(2)}$, $-\chi^{(2)}$, ... goes to : $-\chi^{(2)}$,$+\chi^{(2)}$. This sign change, compensate for the detuned frequencies. In practice at each segment boundary, there are two domains with the same orientation that merge in a single double-as-long domain, as shown in Fig.3.1. In the language of the Bloch sphere, this means that the orientation of the axis of rotation - Ω_R is $\pm|\Omega_R|\hat{x}$. Also, since the design is very similar to a periodic design, with the difference that when new segments begin, a double domain is created, we name this design- composite segmented periodically poled (CSPP).

3.2 CSPP design numerical simulation and experimental measurement

In the following, we present via numerical simulation, the CSPP designs frequency generation capability for two nonlinear processes. The first example, in the CW regime, is for the SFG process. The second example, which was also realized to an experiment, is for a broad SHG process in the ultrashort regime.

3.2.1 CSPP design-numerical simulation in the CW regime

We begin by examining the CSPP designs in the CW regime for two processes. The process that is simulated is SFG, in an Mg-doped $LiNbO_3$ nonlinear crystal with a length L=3.1 mm: 1030

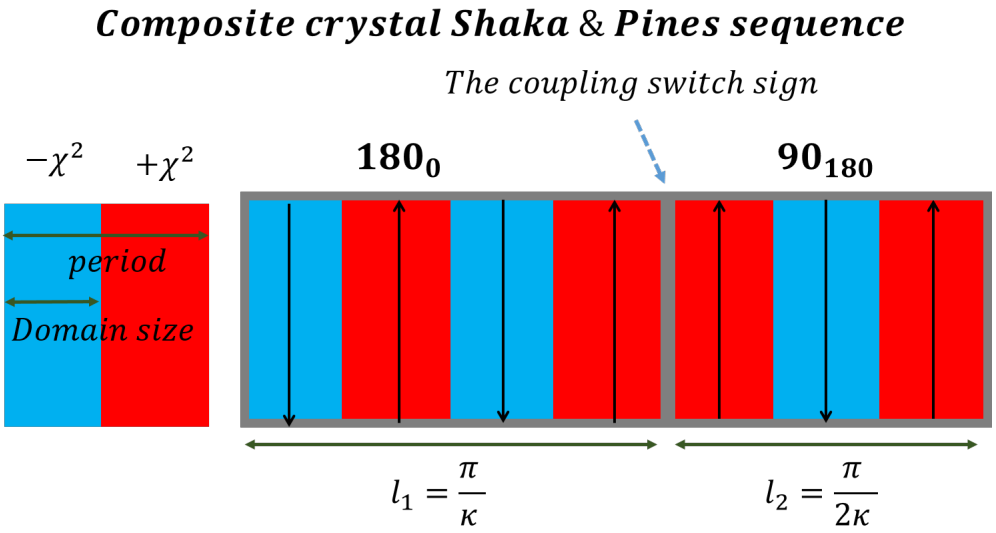

Figure 3.1: Illustration CP in nonlinear crystals. As shown, all the segments are periodically poled with the same period, however, once a new segment begins, the flip order of $\chi^{(2)}$ is changed.

nm as the pump with a broad signal $800\pm20nm$ resulting idler $450\pm7nm$. The pump intensity is 1 $[GW/cm^2]$ and the signal total intensity is 0.1 $[GW/cm^2]$. We will examine this process under four different designs implemented on the crystal. The first three designs are base CSPP, and the length of each segment is detailed in table 3.1, and the fourth design is periodic.

Table 3.1: The CSPP designs 31 segments for each segments the sign of $\chi^{(2)}$ is alter, values taken from Ref. [3].

Segments	Length of the segments [in units of L]
31	0.026;0.045;0.025;0.078;0.023;0.013;0.028; 0.020;0.014;0.023;0.037;0.033;0.070;0.015 0.018;0.031;0.030;0.021;0.051;0.018;0.070; 0.034;0.010;0.023
15	0.0388;0.067;0.076;0.043;0.031;0.116;0.052; 0.076;0.134;0.059;0.048;0.025;0.120;0.064;0.0438
6	0.161;0.174;0.348;0.148;0.083;0.087

We will define the conversion efficiency:

$$\eta = \frac{E_{idler}(z_{out})}{E_{signal}(z_{in})} \tag{3.1}$$

Where z_{out} and z_{in} are the locations of the crystal output and input facets, respectively. In Fig.3.2

(a), the conversion efficiency of the SFG process in the CW regime is shown. We can see that the CSPP31 design (see Table 3.1) - meaning CSPP with 31 segments, produce much broader conversion, whereas the standard periodic design, provide excellent conversion efficiency only for one wavelength.

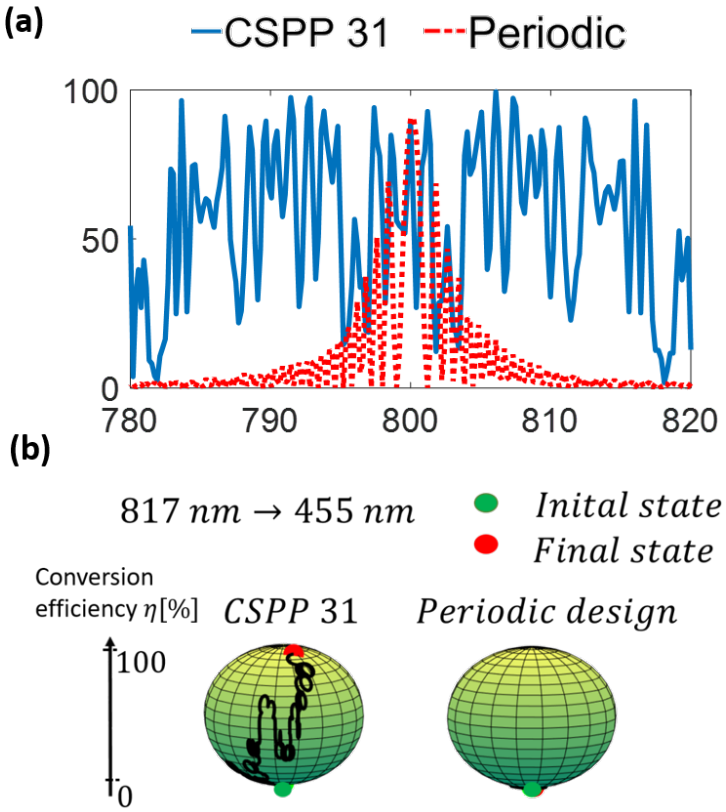

Figure 3.2: Numerical simulation- conversion efficiency of SFG process in the CW regime. (a) The conversion efficiency curve for two designs, 3 mm long: CSPP31 and a periodically poled. (b) The trajectory of a detuned photon on the Bloch sphere, for each of the designs.

In Fig.3.2 (b), we can see the dynamics of the frequency conversion on the Bloch sphere for a detuned photon with wavelength 817 nm (the detuning is zero for 800 nm). By observing the two trajectories of the detuned photon, under CSPP and periodic design respectively, we learn that via the CSPP31 design, the detuned photon reaches almost complete conversion (almost reach the north pole). However, in the case of the periodic design, the radius of the circle of rotation is small due to high detuning, resulting in almost zero conversion.

In Fig.3.3, the efficiency curve of each of the four designs is shown. We can observe that the more segments, the broader the curve. However, there is some amount of trade-off between the efficiency and the bandwidth. Hence, for a signal only 20 nm wide, the CSPP15 will be the

best choice - nearly 100 % efficiency. There are fluctuations in the efficiency curves of the CSPP designs. As will be shown in the following section, in the ultrashort regime, the efficiency curves become smooth, resulting in a broadband conversion bandwidth.

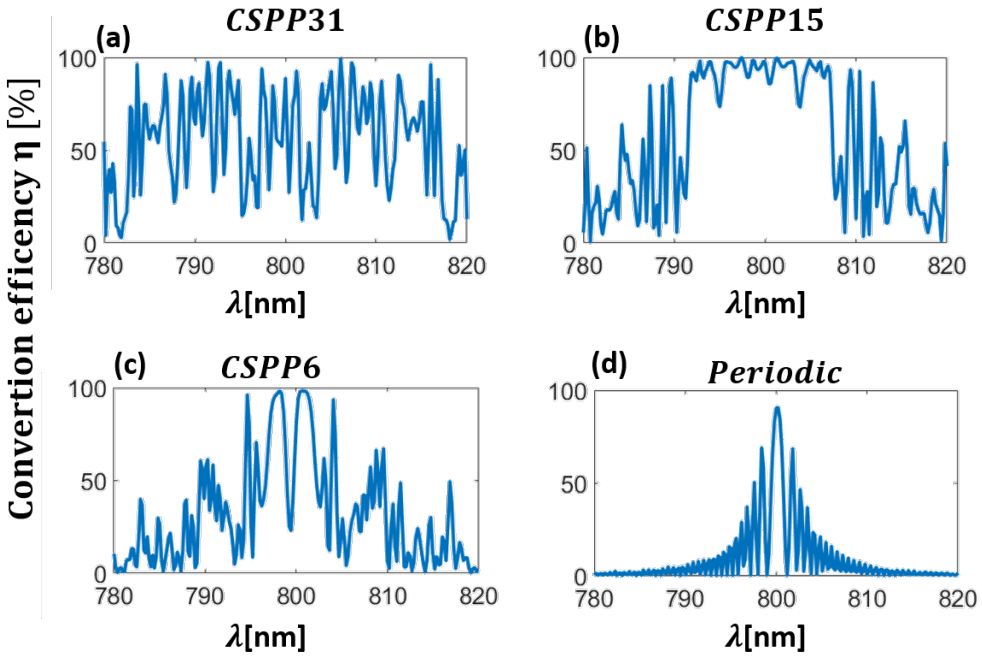

Figure 3.3: Numerical simulation- comparing different CSPP designs in the CW regime for SFG process, $1030+800\pm20$ nm in a Mg-doped $LiNbO_3$ 3mm long crystal. The more segments in the design, the more bandwidth added to the conversion curve (a) CSPP31- 31 segments. (b) CSPP15- 15 segments. (c) CSPP6- 6 segments. (d) Periodic design.

3.2.2 CSPP design-numerical simulation in the ultrashort regime

In this subsection, we will numerically investigate a broad SHG process in the ultrashort regime. The pump, a 100 fs pulse, has an 80 MHz repetition rate pulse at 1030 nm with 20 nm full width half-maximum (FWHM). The pump spectrum was measured and was inserted into the simulation. The spectral efficiency of the pump is defined as follows:

$$S.E = \frac{(P.S - P.R.S)}{(P.S)} \tag{3.2}$$

Where S.E is the spectral efficiency, P.S is the pump spectrum before the crystal and P.R.S is the residual pump spectrum. The crystal is an Mg - doped $LiNbO_3$ 3 mm long. We assume that the spot size is 25 μm, which results in Rayleigh length of about the length of the crystal. It

is important to note again that the simulation assumes planes wave. Therefore, if one wishes to compare experiments results to the simulation, the Rayleigh length has to be at least as long as the crystal. The average power of the pump is 256 ± 5 $[mW]$. This simulates the experiment we later conduct and is detailed in our article.

In Fig.3.4, the conversion curve of the four designs is presented. The designs are: CSPP31, CSPP15, CSPP6 and periodic. We observe that similarly to the CW case, the CSPP31 has the broadest efficiency curve. On the other hand, the highest total efficiency is gained via the CSPP15 design. We can observe that the CSPP designs are superior to the periodic design both in bandwidth and efficiency.

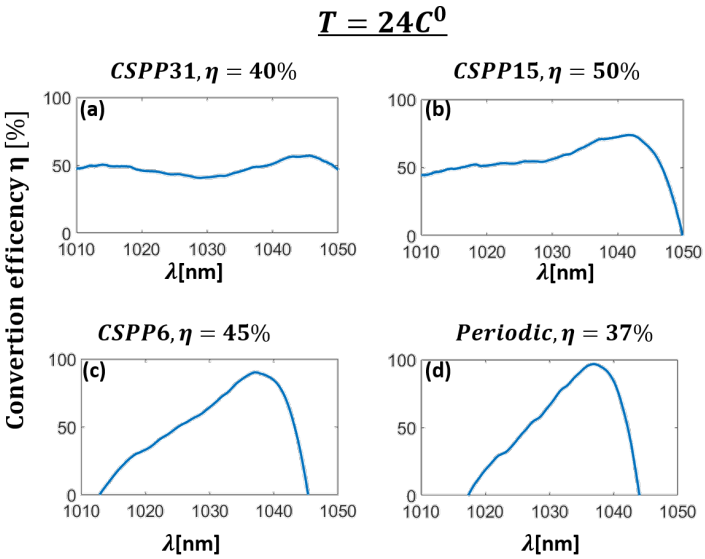

Figure 3.4: Numerical simulation- conversion efficiency of SHG process for pump around 1030 nm, as was measured in the lab, in the ultrashort regime. (a) CSPP31. (b) CSPP15. (c) CSPP6 (d) Periodic design.

Furthermore, we examined the robustness of the designs. In Fig.3.5, the conversion curve of the four designs is presented, at a temperature of $100C^{\circ}$. We can observe that the CSPP31 is entirely robust to the temperature change, and is even more efficient. The periodic design efficiency is severely decreased. We can find that the more segments, the more robust the design are to temperature change.

In our article, which is presented below, we experimentally demonstrate efficient SHG in the ultrashort regime, using CSPP designs -15 and 31. The pump was consisted from an 80 MHz repetition rate pulse at 810 nm with 17.5nm FWHM, originated from the tunable coherent oscillator (Mai Tai), which enters a fs optical parametric oscillator (ORIA IR), which in turn, generate 100 fs pulses - the pump, between 1015-1050 nm with energies 2-6 nJ. The CSPP schemes and a periodically poled design were implemented on Mg-doped $LiNbO_3$ crystal. A broad and efficient

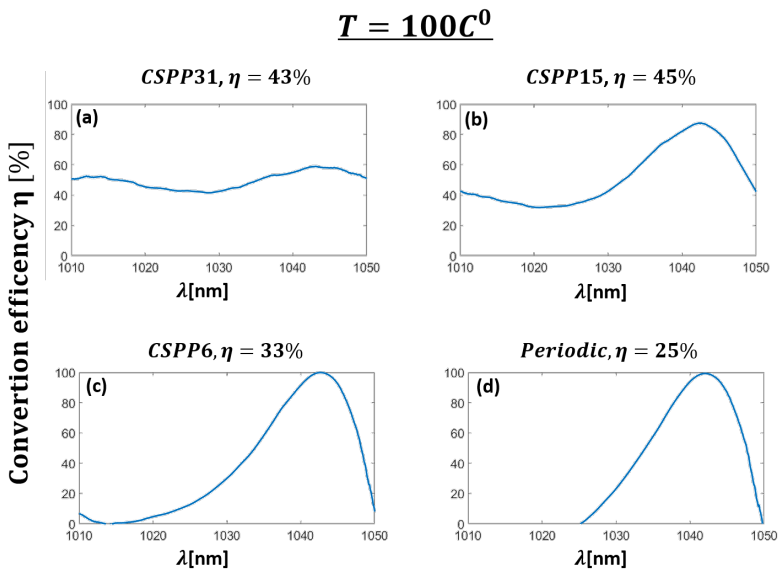

Figure 3.5: Numerical simulation - conversion efficiency of SHG process for pump around 1030 nm, as was measured in the lab, in the ultrashort regime. Examining the design robustness to temperature change, T=100C°. (a) CSPP31. (b) CSPP15. (c) CSPP6 (d) Periodic design.

conversion over a bandwidth of 35 nm was achieved in a rather short crystal length of 3 mm. We demonstrated the CSPP robustness to temperature changes up to 90C°. In correspondence to the numerical simulation, the CSPP performance is superior in all aspects. The experimental results are compared to numerical simulation with excellent agreement.

4 The Article

In the pages below we present our article: ”Robust efficient and broadband SHG of ultrashort pulses in composite crystals”, which was accepted for publication in optics letters.

Optics Letters

Robust, efficient, and broadband SHG of ultrashort pulses in composite crystals

Yonathan Erlich,[1,2] Andon Rangelov,[3] Germano Montemezzani,[4] and Haim Suchowski[1,2,*]

[1]Raymond and Beverly Sackler School of Physics and Astronomy, Tel Aviv University, Ramat Aviv 6779801, Tel Aviv, Israel
[2]Center for Light-Matter Interaction, Tel-Aviv University, Tel-Aviv 6779801, Israel
[3]Department of Physics, Sofia University, James Bourchier 5 blvd., 1164 Sofia, Bulgaria
[4]Supélec, LMOPS, EA 4423, F-57070 Metz, France
*Corresponding author: haimsu@post.tau.ac.il

Received 29 April 2019; revised 24 June 2019; accepted 27 June 2019; posted 27 June 2019 (Doc. ID 365839); published 29 July 2019

We experimentally demonstrate efficient second-harmonic generation (SHG) of tunable ultrashort pulses of 100 femtoseconds, using a novel method based on composite segmented periodically poled (CSPP) design. The scheme was borrowed from the nuclear magnetic resonance (NMR) composite pulses (CP) of Shaka and Pines. Using CSPP, a broadband and efficient conversion over a bandwidth of 35 nm in very short interaction length was achieved. In addition, CSPP showed robustness to temperature changes up to 90°C. Two CSPP schemes with 15 and 31 segments and periodically poled design were implemented on Mg-doped $LiNbO_3$ crystal. The CSPP performance was shown to be superior in all aspects. The experimental results are compared to numerical simulation with excellent agreement.

https://doi.org/10.1364/OL.44.003837

Ultrashort laser pulses are at the heart of ultrafast physics research and applications, as they allow capturing short-time phenomena due to their short time scale, high peak-power intensity, and broad spectral range [1,2]. Combining the high peak power, which allows generation of nonlinear processes, with the simplicity of the second-harmonic generation (SHG) process, makes SHG in the ultrashort regime very popular in a variety of fields, such as nonlinear spectroscopy, metallurgy, photoinduced dynamics in 2D, and condensed matter dynamics and noninvasive background free diagnostics [3–6]. The need for ultrashort pulses in various wavelengths and the fact that some wavelength regions are not easily accessible have suggested the use of frequency conversion schemes to answer this need. In order to achieve efficient and broad frequency conversion, the interacting waves need to be phase matched [7]. The common approaches are birefringence and quasi-phase matching [7]. However, those methods can meet the phase-matching condition only for a specific frequency, preventing the generation of ultrashort pulse. In the past decades, conversion methods for broadband sources were developed, such as short birefringent crystals [8], multi-periodic modulation [9], chirp patterns [10], temperature gradient manipulations [11,12], and randomly oriented crystal [13]. Yet, in these cases, there is usually a tradeoff between bandwidth and efficiency of conversion.

In the last decade, adiabatic frequency conversion has emerged [14,15]. It was demonstrated using this method that the phase-matching condition can be achieved for a wide band of frequencies resulting in high conversion efficiency for a broadband source [16,17]. Adiabatic frequency conversion is based on the fact that the three-wave mixing (TWM) equations, in the approximation of non-depleted pump, has a SU(2) symmetry [14]; therefore, a process such as sum frequency generation (SFG) and difference frequency generation (DFG) can be analog to other physical systems with SU(2) symmetry. In recent years, the adiabatic frequency conversion method was expanded beyond non-depleted pump, in both theory and experiment [16,18–20]. This allowed broad and efficient generation of more processes, such as autoresonance, optical parametric amplification (OPA) and SHG. Though adiabatic frequency conversion allows generating high conversion efficiency from a broad spectral range, it requires a relatively long interaction length [14,15].

Recently, an alternative approach was suggested by Rangelov *et al.* [21]. This approach is based on a CP scheme originated from the field of NMR [22]. CP are sequences that can generate a broad and robust population inversion and are widely implemented in NMR [23]. In their work, they have shown that CP can be used in nonlinear optics, since it relates to a system with SU(2) symmetry. Furthermore, even in the case where the SHG process is in the depleted regime, without SU(2) symmetry, it was suggested that the CP scheme could generate broad and efficient SHG conversion. It is important to mention that there are many CP schemes, but not all of them are suitable for nonlinear crystals. In the nonlinear crystal, the coupling coefficient is proportional to $\chi^{(2)}$, which means it has to be real. Therefore, the relevant CP are those that relate to the coupling coefficient as real. One solution that can generate a broad population inversion and answer these criteria is the CP of Shaka and Pines [24,25], where only the sign of the coupling coefficient is changed. In the context of nonlinear optics, this scheme is called composite segmented periodically poled (CSPP) design. In their work, Rangelov *et al.* demonstrated theoretical and numerical prediction of efficient and

robust frequency conversion via CSPP crystal in the CW regime [21], yet no experimental observation has been performed, and no numerical simulation in the ultrashort regime was demonstrated.

In this Letter, we experimentally demonstrate high-efficiency, robust, and broadband SHG for ultrashort pulses via CSPP designs on a nonlinear crystal [24,25] and compare their performance to the periodic design. We show that for a pump pulse of 100 fs, with pulse energies in the regime of nano-Joule, the SHG conversion efficiency can reach 50%. Moreover, we show that the CSPP designs are robust to temperature changes of more than 90°C and are efficient within a bandwidth of 35 nm. In addition, we have compared our experimental results to our numeric simulation, which takes into account dispersion effects and higher-order nonlinear parasitic effects, as was developed by Dahan *et al.* [16,17].

The experiment setup is shown in Fig. 1(a). An 80 MHz repetition rate pulse at 810 nm with 17.5 nm full width half-maximum (FWHM), originated from a tunable coherent oscillator (Mai Tai), enters a fs optical parametric oscillator (ORIA IR), which, in turn, generates 100 fs pulses between 1015–1050 nm with energies 2–6 nJ. The pump pulse passes through a $\lambda/2$ wave plate to rotate the polarization to the extraordinary axis of the crystal and a neutral density (ND) filter that allows manipulating the pump power. The pump is focused via a 30 mm focal length lens into a Mg-doped $LiNbO_3$ nonlinear crystal with a length $L = 3.1$ mm. The fabricated crystal has three designs: two are based on CSPP design, with 15 and 31 sequences, and a controlled periodic poled design. The CSPP was designed as follows, the period of the flip sign of the $\chi^{(2)}$ was such that the phase mismatch for 1030 nm was zero, similar to the periodic case, resulting in a period of

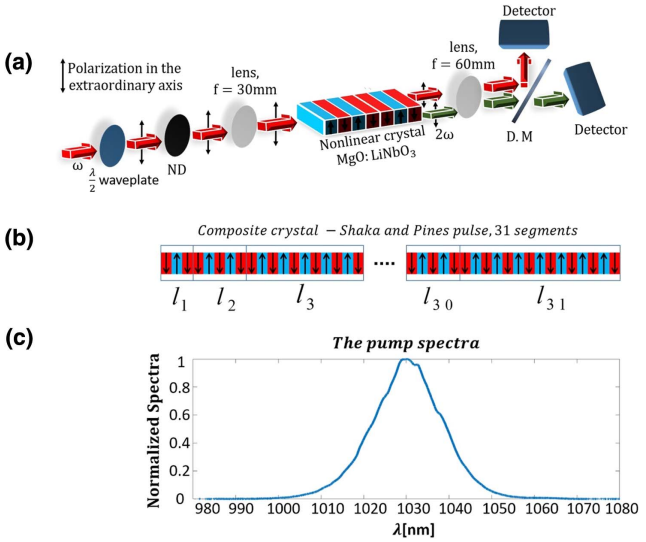

Fig. 1. Composite pulses (CPs) experiment. (a) Experiment setup: $\lambda/2$ wave plate, neutral density filter (ND), lens with 30 mm focal length, nonlinear crystal, Mg-doped $LiNbO_3$, with three designs: two CSPP designs, with 15 and 31 segments and a periodic designs, lens with 60 mm focal length and a dichroic mirror (DM). (b) Scheme of the Shaka and Pines design for 31 segments. As shown, all segments are periodically poled with the same period; however, once a new segment begins, the flip order of $\chi^{(2)}$ is changed. (c) Spectrum for a pump centered around 1030 nm.

$\Lambda = 6.3$ μm. However, in contrast to the periodic design, in the CSPP, once a new sequence begins, the coupling coefficient switches its signs, resulting in a change in the flip order: $\chi^{(2)}+$, $\chi^{(2)}-$, … goes to: $\chi^{(2)}-$, $\chi^{(2)}+$. In practice, at each segment boundary, there are two domains with the same orientation that merge in a single double-as-long domain, as shown in Fig. 1(b). Table 1 shows the segment distributions of the two CSPP designs. After the pump passes through the crystal, a 60 mm focal length lens collects the pump and the signal. A dichroic mirror (DM) around 650 nm separates the pump and the SHG signal. The spectrum of the SHG pulse was measured using an Ocean spectrometer, whereas the pump pulse spectrum was measured using a Yokogawa spectrometer. Also, the nonlinear crystal was placed in a homemade oven, which allowed sample heating up to 90°C. The average power for the SHG was measured after the DM.

Our analysis takes into consideration the losses due to Fresnel reflection. Also, we calculated the spectral efficiency of the pump, which is defined as follows:

$$\text{S.E} = \frac{(\text{P.S} - \text{P.R.S})}{(\text{P.S})}, \tag{1}$$

where S.E is the spectral efficiency, P.S is the pump spectrum before the crystal, and P.R.S is the pump residual spectrum. The TWM simulation is in the full nonlinear dynamical regime, as developed by Dahan *et al.* [16,17], and in the simulation, the two-photon absorption (TPA) is taken into account, as in previous experiments [16,17]. It is worth noting that in our case, since the peak intensities are very high, up to 3 GW/cm^2, the TPA process is highly dominant. The conversion efficiency is defined as follows:

$$\eta = \frac{E_{\text{SHG}}(z_{\text{out}})}{E_P(z_{\text{in}})}, \tag{2}$$

where z_{out} and z_{in} are the locations of the crystal output and input facets, respectively. In our experimental observation, we have examined the performance of the CSPP designs as a function of the following parameters: the pulse centered wavelength, pulse energy, and crystal temperature. Also, we examined the conversion efficiency of each of the three designs. In addition, for a pulse centered around 1030 nm, as shown in Fig. 1(c), we compared the SHG of each design. Both the spectral efficiency and the temperature robustness measurements of the 31 segments design were compared to the simulation. In each parameter, the performance of the composite crystals was compared experimentally to a periodically poled design.

Table 1. The CP Designs, 15 and 31 Segments. For Each Segment, the Sign of $\chi^{(2)}$ is Altered. Values Taken From [24,25].

Segments	Length of the Segments [in units of L]
15	0.039; 0.067; 0.077; 0.043; 0.031; 0.116; 0.052; 0.077; 0.134; 0.06; 0.049; 0.026; 0.12; 0.064; 0.044
31	0.014; 0.072; 0.063; 0.022; 0.016; 0.035; 0.021; 0.026; 0.045; 0.025; 0.078; 0.023; 0.013; 0.028; 0.020; 0.014; 0.023; 0.037; 0.033; 0.070; 0.015 0.018; 0.031; 0.030; 0.021; 0.051; 0.018; 0.070; 0.034; 0.010; 0.023

In Fig. 2(a), we show the SHG efficiency for eight different pump pulses, where each is a 20 nm FWHM pulse around a given wavelength. We observe a high broadband acceptance of the design of the 31 segments, up to 45% efficiency from 1015 nm up to 1050 nm pulses, where the periodic design produces good efficiency only for 1030 nm pump pulse and its efficiency strongly decreases afterward. By comparing the 15 and 31 segment designs, we learn that as the number of segments is increased, the bandwidth acceptance is increased accordingly, from 20–35 nm. In Fig. 2(b), the normalized SHG spectrum from a pulse centered around 1030 nm is shown. As can be seen, the CSPP SHG is much broader then the periodic design, and the more segments, the wider its SHG spectrum. In Fig. 2(c), the temperature robustness of the three designs is tested; the crystal is heated to 90°C, and the SHG efficiency for pump centered around 1030 nm is measured. Both CSPP designs demonstrate robustness to temperature changes and even an increase in conversion efficiency is observed, while the efficiency of the periodic design decreases with the heating of the nonlinear crystal. Figure 2(d) illustrates the SHG efficiency of a pump at 1030 nm, as a function of pump energy measurements. The response is approximately the same for all designs; all show efficiency around 40%–50%, where we can see that the 15 segments design has the highest conversion efficiency, up to 50%. We learn that a CSPP is robust to temperature changes, and with a high number of segments, it can generate a broad SHG in an ultrashort time scale.

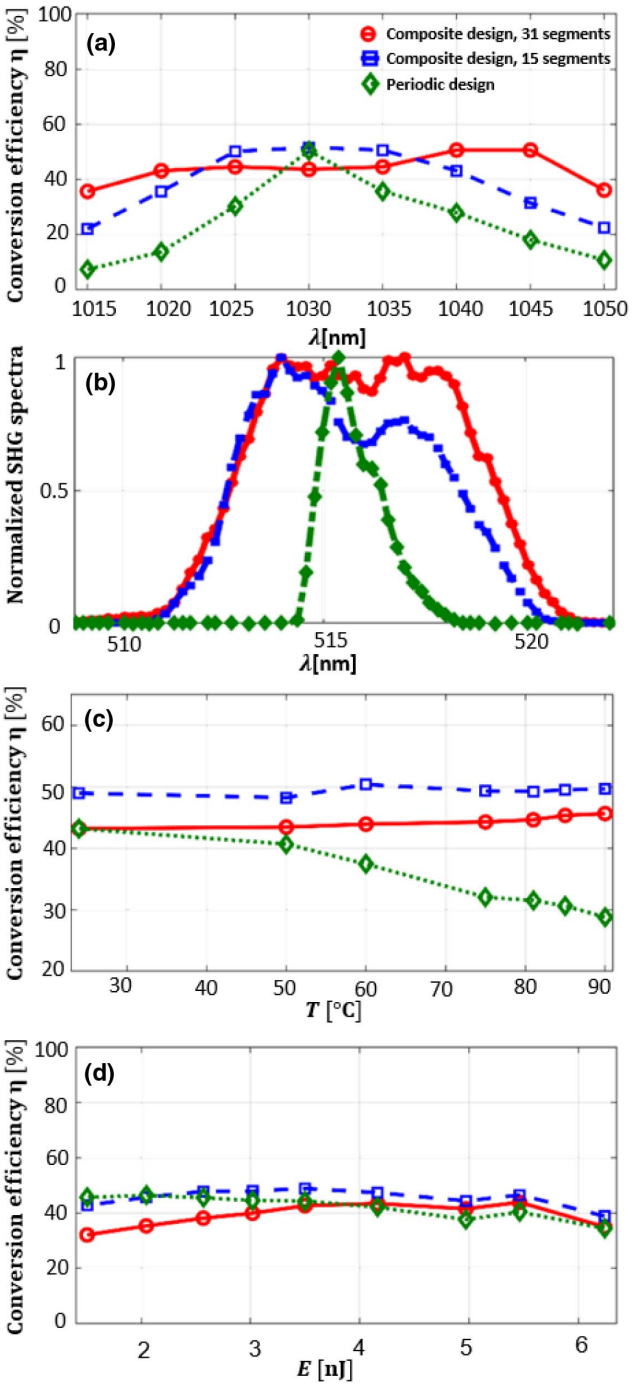

Fig. 2. Comparison between the CSPP designs and the periodic design. (a) Conversion efficiency of ultrashort pulses centered around different wavelengths. (b) Normalized SHG spectrum of each design. (c) Conversion efficiency of each design as a function of crystal temperature. (d) Conversion efficiency of each design as a function of the pulse energy, for a pulse centered around 1030 nm.

In addition, we compared our experimental results to numerical simulation, using the approach detailed in Refs. [16,17], which allows to predict the nonlinear interaction for the CSPP design in the ultrashort regime. In Fig. 3(a), the residual pump spectrum measurements and simulation are shown; we can see very good agreement. From the residual pump spectrum, the spectral efficiency can be calculated according to Eq. (1). We can observe a disagreement in the tail of the spectrum, and therefore we can expect disagreement in the spectral efficiency outside the FWHM of the pump. In Fig. 3(b), the spectral efficiency of the 31 segments design measurements and simulation is shown. The spectral efficiency of the 31 segments is very broad, spanning around 35 nm, and has

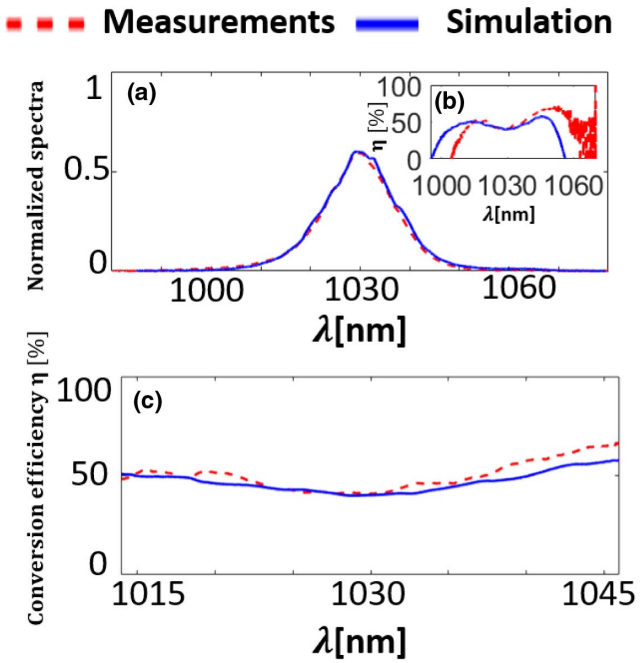

Fig. 3. (a) Measurements and simulation for the residual pump around 1030 nm with energy 3.2 nJ. (b) Measurements and simulation of the spectral efficiency according to Eq. (1). (c) Spectral efficiency in the FWHM.

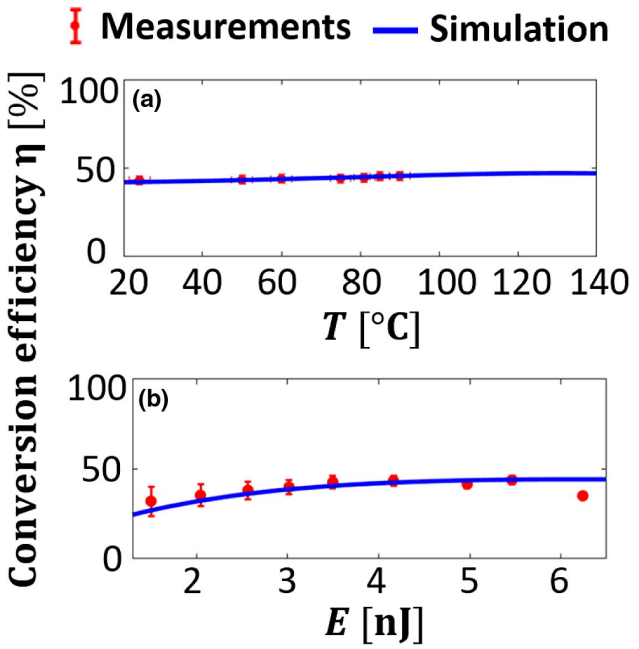

Fig. 4. Simulation of the CSPP with 31 segments with comparison to the experiment results. (a) Simulation of the temperature robustness versus experimental results. (b) Simulation of the conversion efficiency as a function of pulse energy.

up to 45% conversion efficiency. The partial agreements outside the FWHM can be explained by the fact that outside the FWHM, due to low photon flux, the background noise can cause inaccuracies in the spectrometer measurement, as shown in the tail of the spectrum in Fig. 3(a). In Fig. 3(c), the spectral efficiency in the FWHM is presented. We can observe excellent agreement between the simulation and the experiment.

Figure 4(a) shows the temperature robustness of the 31 segments design measurements and the simulation results; very good agreement is shown. We can observe that the temperature robustness theoretically holds beyond 90°C. We note that in our simulation, we took into account the effective nonlinear susceptibility, d_{33}, dependence on the temperature, according to Miller's rule [26]:

$$d_{33} = \Delta_{\text{Miller}}[n(\omega, T)^2 - 1]^2[n(2\omega, T)^2 - 1], \quad (3)$$

where Δ_{Miller} is Miller's delta according to [26], and $n(\omega, T)$ is the index of refraction as a function of the temperature T and the frequency ω. In Fig. 4(b), the measurements and the simulation results of the conversion efficiency as a function of the pulse energy are shown. We can observe very good agreement between the results and the simulation, besides one point. We observe a decrease in conversion efficiency, deviating from the numerical prediction. We attribute this to a more parasitic process, which was not taken into account and is relevant in the strong pump regime, such as the change in the index of refraction and three-photon absorption.

In conclusion, in this experiment, we demonstrated both experimentally and numerically a new method to achieve high conversion efficiency for ultrashort pulses in relatively short nonlinear crystals. The 31 CSPP delivers high efficiency for a bandwidth of 35 nm, allowing a potential platform for efficient ultrashort conversion of pulses as short as 25 fs. In addition, the CSPP shows robustness to temperature changes. The CSPP design advantage lies in the fact that it can supplement the adiabatic scheme in regimes where not a very broad bandwidth is required. Then there is no need for a long crystal to achieve high efficiency, which makes the TPA process less dominant due to shorter absorption length. Moreover, the design technique is rather easy to implement on crystals, since it requires the same periodicity of a periodic design with the change in the sign of $\chi^{(2)}$ between neighboring crystal segments [21]. We believe that this new method might be useful for broadband upconversion imaging. While we used the CSPP scheme for the SHG process, CSPP could be used to generate efficient and broad conversion for more processes, such as SFG, DFG, and OPA.

Funding. H2020 European Research Council (ERC) (MIRAGE 20-15, 639402).

REFERENCES

1. R. J. Lanzafame, Photomed. Laser Ther. **25**, 58 (2007).
2. A. H. Zewail, Angewandte Chemie Int. Ed. **39**, 2586 (2000).
3. M. Fiebig, V. V. Pavlov, and R. V. Pisarev, J. Opt. Soc. Am. B **22**, 96 (2005).
4. R. M. Corn and D. A. Higgins, Chem. Rev. **94**, 107 (1994).
5. F. Helmchen and W. Denk, Nat. Methods **2**, 932 (2005).
6. P. J. Campagnola and L. M. Loew, Nat. Biotechnol. **21**, 1356 (2003).
7. R. W. Boyd, *Nonlinear Optics* (Elsevier, 2003).
8. H. Suchowski, B. D. Bruner, A. Arie, and Y. Silberberg, Opt. Photon. News **21**(10), 36 (2010).
9. D. S. Hum and M. M. Fejer, C. R. Physique **8**, 180 (2007).
10. T. Suhara and H. Nishihara, IEEE J. Quantum Electron. **26**, 1265 (1990).
11. Y. L. Lee, Y.-C. Noh, C. Jung, T. J. Yu, D.-K. Ko, and J. Lee, Opt. Express **11**, 2813 (2003).
12. K. Regelskis, J. Želudevičius, N. Gavrilin, and G. Račiukaitis, Opt. Express **20**, 28544 (2012).
13. M. Baudrier-Raybaut, R. Haidar, P. Kupecek, P. Lemasson, and E. Rosencher, Nature **432**, 374 (2004).
14. H. Suchowski, G. Porat, and A. Arie, Laser Photon. Rev. **8**, 333 (2014).
15. H. Suchowski, D. Oron, A. Arie, and Y. Silberberg, Phys. Rev. A **78**, 063821 (2008).
16. A. Dahan, A. Levanon, M. Katz, and H. Suchowski, J. Phys. Condens. Matter **29**, 084004 (2017).
17. A. Levanon, A. Dahan, A. Nagler, E. Lifshitz, E. Bahar, M. Mrejen, and H. Suchowski, Opt. Lett. **42**, 2992 (2017).
18. G. Porat, J. Opt. Soc. Am. B **30**, 1342 (2013).
19. C. Phillips, C. Langrock, D. Chang, Y. Lin, L. Gallmann, and M. Fejer, J. Opt. Soc. Am. B **30**, 1551 (2013).
20. A. Leshem, G. Meshulam, G. Porat, and A. Arie, Opt. Lett. **41**, 1229 (2016).
21. A. Rangelov, N. Vitanov, and G. Montemezzani, Opt. Lett. **39**, 2959 (2014).
22. M. Levitt, J. Magn. Reson. **33**, 473 (1979).
23. J. Keeler, *Understanding NMR spectroscopy* (Wiley, 2011).
24. A. Shaka, Chem. Phys. Lett. **120**, 201 (1985).
25. A. Shaka and A. Pines, J. Magn. Reson. **71**, 495 (1987).
26. I. Shoji, T. Kondo, A. Kitamoto, M. Shirane, and R. Ito, J. Opt. Soc. Am. B **14**, 2268 (1997).

5 Summary and further outlook

In this research, we have investigated a new scheme for frequency conversion that is both broad and efficient. We examined our new scheme - CSPP, both numerically and experimentally. We found numerically that using CSPP design, broad robust and efficient frequency conversion can be achieved both in the CW regime and in the Ultrafast regime in a short interaction length. Furthermore, we demonstrated experimentally a highly broad efficient and robust SHG of the ultrashort pulse at 100 fs in a rather short crystal length. We emphasize that this method is very general and can further be exploit into more processes, such as SFG, DFG, and OPA. We believe that this scheme supplements the adiabatic scheme, by offering more solutions to overcome the efficiency bandwidth tradeoff in a short crystal length. This research opens the door to exploit more schemes from NMR and other fields to be implemented not only for nonlinear crystal but for fibers as well, for broad and efficient frequency conversion.

References

[1] Trebino. Trebino lectures, http://frog.gatech.edu/lectures.html.

[2] Haim Suchowski, Gil Porat, and Ady Arie. Adiabatic processes in frequency conversion. *Laser and Photonics Reviews*, 8(3):333–367, 2014.

[3] AJ Shaka and A Pines. Symmetric phase-alternating composite pulses. *Journal of Magnetic Resonance (1969)*, 71(3):495–503, 1987.

[4] Robert W Boyd. *Nonlinear Optics*. Elsevier, 2003.

[5] Haim Suchowski, Barry D Bruner, Ady Arie, and Yaron Silberberg. Broadband nonlinear frequency conversion. *Optics and Photonics News*, 21(10):36–41, 2010.

[6] David S Hum and Martin M Fejer. Quasi-phasematching. *Comptes Rendus Physique*, 8(2):180–198, 2007.

[7] Toshiaki Suhara and Hiroshi Nishihara. Theoretical analysis of waveguide second-harmonic generation phase matched with uniform and chirped gratings. *IEEE Journal of Quantum Electronics*, 26(7):1265–1276, 1990.

[8] Kestutis Regelskis, J Želudevičius, N Gavrilin, and G Račiukaitis. Efficient second-harmonic generation of a broadband radiation by control of the temperature distribution along a nonlinear crystal. *Optics Express*, 20(27):28544–28556, 2012.

[9] M Baudrier-Raybaut, R Haidar, Ph Kupecek, Ph Lemasson, and E Rosencher. Random quasi-phase-matching in bulk polycrystalline isotropic nonlinear materials. *Nature*, 432(7015):374, 2004.

[10] Andrew M Childs, Edward Farhi, and John Preskill. Robustness of adiabatic quantum computation. *Physical Review A*, 65(1):012322, 2001.

[11] Albert Messiah. Quantum mechanics, volume ii. *Appedix C (Section IV)(North-Holland Publishing Company, Amsterdam, 1969)*, 1962.

[12] Asaf Dahan, Assaf Levanon, Mordechai Katz, and Haim Suchowski. Ultrafast adiabatic second harmonic generation. *Journal of Physics: Condensed Matter*, 29(8):084004, 2017.

[13] Assaf Levanon, Asaf Dahan, Achiya Nagler, Erga Lifshitz, Eyal Bahar, Michael Mrejen, and Haim Suchowski. Pulse shaping of broadband adiabatic shg from a ti-sapphire oscillator. *Optics letters*, 42(15):2992–2995, 2017.

[14] Leslie Allen and Joseph H Eberly. *Optical resonance and two-level atoms*, volume 28. Courier Corporation, 1987.

[15] AA Rangelov, NV Vitanov, and G Montemezzani. Robust and broadband frequency conversion in composite crystals with tailored segment widths and χ (2) nonlinearities of alternating signs. *Optics Letters*, 39(10):2959–2962, 2014.

[16] Felix Bloch. Nuclear induction. *Physical review*, 70(7-8):460, 1946.

[17] Richard P Feynman, Frank L Vernon Jr, and Robert W Hellwarth. Geometrical representation of the schrödinger equation for solving maser problems. *Journal of applied physics*, 28(1):49–52, 1957.

[18] Haim Suchowski, Dan Oron, Ady Arie, and Yaron Silberberg. Geometrical representation of sum frequency generation and adiabatic frequency conversion. *Physical Review A*, 78(6):063821, 2008.

[19] MH Levitt. Mh levitt and r. freeman, j. magn. reson. 33, 473 (1979). *J. Magn. Reson.*, 33:473, 1979.

[20] James Keeler. *Understanding NMR spectroscopy*. John Wiley & Sons, 2011.

[21] AJ Shaka. Composite pulses for ultra-broadband spin inversion. *Chemical Physics Letters*, 120(2):201–205, 1985.

Appendices

A Deriving the three wave equations

The Maxwell equations:

$$\nabla \cdot D = \rho \tag{A.1}$$

$$\nabla \cdot B = 0 \tag{A.2}$$

$$\nabla \times E = -\frac{\partial B}{\partial t} \tag{A.3}$$

$$\nabla \times H = \frac{\partial D}{\partial t} + J \tag{A.4}$$

We will assume the following: no free charges - $\rho = 0$, no free current - $J = 0$ and non magnetic media - $B = \mu_0 H$. D and E relates in the following manner:

$$D = \varepsilon_0 E + P^1 + P^{NL} \tag{A.5}$$

where the polarization was divided into two terms: linear with the electric field and nonlinear. By taking curl to the third Maxwell equation and by using the above equation with the vector identity $\nabla \times \nabla \times E = \nabla(\nabla \cdot E) - \nabla^2 E$, the wave equation is derived:

$$\nabla^2 E - \frac{1}{c^2}\frac{\partial^2}{c^2 \partial t^2} E = \frac{1}{\varepsilon_0 c^2}\frac{\partial^2}{^2 \partial t^2}(P^1 + P^{NL}) \tag{A.6}$$

Using equation 1.2, we see that $P^1 = \chi^1 E$, therefore the wave equation takes the form:

$$\nabla^2 E - \frac{\varepsilon^1}{c^2}\frac{\partial^2}{\partial t^2} E = \frac{1}{\varepsilon_0 c^2}\frac{\partial^2}{\partial t^2}(P^{NL}) \tag{A.7}$$

Where $\varepsilon^{(1)} = 1 + \chi^{(1)}$, is the relative permittivity, which relates to the index of refraction in the following manner: $\varepsilon^{(1)} = n^2$. This equation has the form of a driven wave equation. Where the source term is the nonlinear polarization. If the electric field and the polarization can be

decompose to sum of plane waves, each with different frequency, than for each frequency, the following equation will hold:

$$\nabla^2 E_n(\mathbf{r}) + \frac{\varepsilon^{(1)}\omega_n^2}{c^2}\frac{\partial^2}{\partial t^2}E_n(\mathbf{r}) = -\frac{\omega_n^2}{\varepsilon_0 c^2}\frac{\partial^2}{\partial t^2}(P_n^{NL}(\mathbf{r})) \tag{A.8}$$

B Two level system - mathematical analysis

In the absence of external field, the electron Hamiltonian [14]:

$$H_0 = \varepsilon_1 |e_1><e_1| + \varepsilon_2 |e_2><e_2| \tag{B.1}$$

Where ε_1 is the energy of the ground state, ε_2 is the energy of the excited state, $|e_1>$ and $|e_2>$ are respectively the eigenstate of the ground and excited state. In the presence of an electric field of the form: $E = E_0 cos(\omega t + \phi)\hat{n}$, the Hamiltonian becomes time dependent in the following way [14]:

$$H(t) = \varepsilon_1 \hat{N_1} + \varepsilon_2 \hat{N_2} - \frac{\hbar \Omega_R}{2} cos(\omega t + \phi)[\hat{\sigma_-} + \hat{\sigma_+}] \tag{B.2}$$

Where we defined: $\hat{N_1} = |e_1><e_1|, \hat{N_2} = |e_2><e_2|$ and $\hat{\sigma_-} = |e_1><e_2|, \hat{\sigma_+} = |e_2><e_1|$.

In order to solve the schrdinger equation: $i\hbar \frac{d|\psi(t)>}{dt} = \hat{H}|\psi(t)>$, we will assume the following form of solution:

$$|\psi(t)> = c_1(t) e^{-i\frac{\varepsilon_1 t}{\hbar}} |e_1> + c_2(t) e^{-i\frac{\varepsilon_2 t}{\hbar}} |e_2> \tag{B.3}$$

Before we continue to solve the equation, we will apply the rotating wave approximation. Terms with high oscillations, of the form $e^{-it(\omega + \frac{\varepsilon_1 t}{\hbar})}$, will be neglected in respect to terms with small oscillations: $e^{-it(-\omega + \frac{\varepsilon_1}{\hbar})}$. Therefore under this approximation, the Hamiltonian can be written in the following manner:

$$H(t) = \varepsilon_1 \hat{N_1} + \varepsilon_2 \hat{N_2} - \frac{\hbar \Omega_R}{2} [e^{i\omega t + i\phi} \hat{\sigma_-} + e^{-i\omega t - i\phi} \hat{\sigma_+}] \tag{B.4}$$

applying this Hamiltonian from the above equation, the equations for the coefficients are:

$$\frac{dc_1(t)}{dt} = i\frac{\Omega_R}{2} c_2(t) e^{-i\frac{\Delta t}{\hbar} + i\phi} \tag{B.5}$$

$$\frac{dc_2(t)}{dt} = i\frac{\Omega_R}{2}c_1(t)e^{+i\frac{\Delta t}{\hbar}-i\phi} \tag{B.6}$$

where $\Omega = \sqrt{\Omega_R^2 + (\Delta/\hbar)}$ and the detuning, Δ is defined as: $\Delta = \varepsilon_2 - (\varepsilon_1 + \hbar\omega)$. Solving the two coupled equations, under the assumption that the system is initially in the ground state, we get the following [14]:

$$c_1(t) = e^{i\frac{-\Delta t}{2\hbar}}[cos(\frac{\Omega t}{2}) + i\frac{\Delta}{\Omega\hbar}sin(\frac{\Omega t}{2})] \tag{B.7}$$

$$c_2(t) = e^{i\frac{\Delta t-\phi}{2\hbar}}[i\frac{\Omega_R}{\Omega}sin(\frac{\Omega t}{2})] \tag{B.8}$$

אוניברסיטת תל אביב
TEL AVIV UNIVERSITY

הפקולטה למדעים מדויקים ע"ש ריימונד ובברלי סאקלר

בית הספר לפיסיקה ואסטרונומיה

המחלקה לחומר מעובה

המרת תדר רחבת סרט בעזרת סכמות של אותות מורכבים

חיבור זה מוגש כחלק מהדרישות לקבלת תואר 'מוסמך למדעים' באוניברסיטת תל אביב

על ידי

יונתן ארליך

עבודה זו הוכנה בהנחיתו של

ד"ר חיים סוכובסקי

אוגוסט 2019

תקציר

לייזרים פולסים אולטרה קצרי זמן, נמצאים במוקד המחקר של שדות רבים בפיזיקה, זאת בשל הרזולוציה הזמנית שלהם, עוצמת הפולס ורוחב הסרט שלהם. עוצמת הפולס בשילוב עם הפשטות ביצירת תהליך של הרמוניה שנייה SHG, הופך את התהליך הנ"ל- SHG לפופלרי מאד במגוון שדות מחקר כגון ספקטרוסקופיה לא לינארית ומערכות הדמיה. הצורך במקורות לייזרים פולסים אולטרה קצרי זמן והעובדה שקיימים אורכי גל שאינם נגישים בקלות, גרמו לחוקרים רבים להשתמש בסכמות המרת תדר. לרוב, סכמות אלו יכולות לאפשר המרה רחבת סרט אך במחיר של יעילות, או שהן צורכות אורך אינטרקציה משמעותי.

במחקר שלנו, אנו חוקרים סקיצה חדשה להמרת תדר רחבה ויעילה. אנו מדגימים באופן נומריי וניוסויי, המרת הרמוניה שנייה רחבת סרט, מלייזר פולסי של 100 פמטו שניות, בעזרת סכמה, שמבוססת על אותות מורכבים על גביש מהודנס בצורה פירודית למקוטעים -CSPP. הסכימה לקוחה מתחום שדה התהודה המגנטית. לצורך ביצוע הסימולציה הנומרית במשטר האולטרה מהיר, השתמשנו בסימולצה חדשית שפותחה במעבדה שלנו. בעזרת סכמה זו -CSPP, הושגה המרה רחבת סרט של עד 35 ננו מטר באורך אינטקציה קצר מאד. יתר על כך, התכנון CSPP מראה עמידות לשינויי טמפרטורה. בנוסף תוצאות הניסויי מושוואות לחישובים נומריים, עם התאמה מעולה ותכנון ה CSPP מראה עליונות בביצועים ביחס לתכנון פיריודי סטנדרטי. מעבר לעובדה שהסקיצה החדשה שמצאנו יכולה לשמש להמרת תדר רחבה ויעילה במגוון תהליכים לא לינאריים, היא גם מוכיחה את הפוטנציאל הגלום בניצול סקיצות של אותות מרוכבים לתחום של אופטיקה לא לינארית.